Department of Physics and Astronomy
University of Heidelberg

Bachelor Thesis in Physics
submitted by

Matthias Berg

born in Göttingen (Germany)

2022

Tomographic reconstruction of photoelectron momentum distribution obtained through Velocity Map Imaging with a 100 MHz laser in a femtosecond enhancement cavity

This Bachelor Thesis has been carried out by Matthias Berg at the
Max Planck Institute for Nuclear Physics in Heidelberg
under the supervision of
apl. Prof. José R. Crespo López-Urrutia

Abstract

A velocity map imaging setup has been designed and fabricated at the Max Planck Institute for Nuclear Physics in Heidelberg to study multiphoton ionization. This setup is placed in an optical cavity to amplify a frequency comb used to generate the photoelectrons. A rotatable wave plate can be used to change the polarization of the laser, by changing the polarization it is possible to view the electron momentum distribution from different angles. In this work, first measurements with this setup were investigated, and the resulting electron momentum distribution was reconstructed as a 3D model using the Abel transform and computed tomography.

Zusammenfassung

Zur Untersuchung von Multiphoton Ionisation ist am Max-Planck-Institut für Kernphysik in Heidelberg ein Velocity Map Imaging Aufbau entworfen und hergestellt worden. Dieser Aufbau befindet sich in einer optischen Kavität zur Verstärkung eines Frequenzkammes, mit dem die Photoelektronen erzeugt werden. Mit einer drehbaren Wellenplatte kann die Polarisation des Lasers verändert werden. Durch die Änderung der Polarisation ist es möglich die Elektronenimpulsverteilung aus verschiedenen Winkeln zu betrachten. In dieser Arbeit wurden erste Messungen mit diesem Aufbau untersucht und die entstandene Elektronenimpulsverteilung mit Hilfe der Abel Transformation und von Computer Tomographie als 3D-Modell rekonstruiert.

Contents

1 Motivation

"Somewhere, something incredible is waiting to be known." Carl Sagan

We humans strive towards great things and to comprehend the world we live in better and better. The unknown motivates us to learn more and to discover 'something incredible', therefore we push our boundaries and the limitations and expand the field of our knowledge, and what we do not understand we aim to understand.

In physics, we do not only focus on new undiscovered phenomena, but we want to deepen what we know. In the end of the 19th century, the discovery of the photoelectric effect [14] started the rise of quantum physics and helped to get a deeper understanding of electrodynamics, nuclear physics and several more research areas. Therefore, it had an impact on all the areas of physics [23]. The discovery of the laser in 1960 [22] was a huge improvement for the scientific world and allowed to research more precisely and to investigate new areas of physics and to prove quantum dynamics with an extremely good precision. With the help of the laser, many natural constants were determined and the ionization process was examined more accurately. Especially in the process of studying multi photoionization, the laser proved to be essential. Through the realization of the frequency comb [32], it became possible to measure out the absolute frequencies of light, which helps enormously to quantify exact natural constants. The product imaging technique made it possible to capture images of the ionization, at least the momentum distribution of photoelectrons [11]. Eppink and Parker evolved this technique with Velocity Map Imaging (VMI)[15]. VMI allows detecting momentum distribution without affecting the momentum of the photoelectrons. Photoelectrons provide a lot of information of the atoms and energy of the energy shells [31]. The usual approach to examine photoelectrons is to use the cylindrical symmetry of the momentum distribution and to use the Abel transform in order to reconstruct the electron clouds. In this thesis, this method is compared with a different approach namely tomographic reconstruction, through the change of the polarization of the laser it is possible to change the direction of the momentum of the electrons in the ionization process. Therefore, the polarization determines the angle under which angle the photoelectron momentum distribution is projected on the detector. These asymmetric projections were measured with a VMI setup and by computer tomography it is possible to reconstruct the electron momentum distribution without dependence on the symmetry of the distribution, as it would be the case with the Abel transform.

Thesis Outline

The second chapter provides an explanation of the theoretical background of computer tomography and the Abel transform. The physics behind multi photoionization and the femtosecond enhancement cavity are explained in the second chapter as well. In the next chapter the experimental setup is described. In the following chapter the results of the measurement are presented and evaluated, the computer tomography and the Abel transform are demonstrated on the measured images and the reconstruction methods are compared to each other.

2 Theory

In this chapter, the theoretical background is explained by giving an overview of the theory. The first part is an introduction into reconstruction methods, especially into tomography and into the Abel transform. In the second part, photoionization is explained due to which the electron momentum distribution occur. At last, a theoretical description of the frequency comb and the femtosecond enhancement cavity is given.

2.1 3D-reconstruction

There are several options for the reconstruction of a 3D-model, however in this section Abel transform and tomography will be investigated.

2.1.1 Tomography

Tomography is the way of reconstruction with the help of several 2D-projections of the object via filtered backprojection (FBP), which will be explained in the following. The mathematical background is oriented on [8].

Filtered Backprojection

The filtered backprojection is a method to generate an image of an object and its interior. To make a filtered backprojection, the density of an object is measured as a projection from different angles. With the projections from all around the object, it is possible to calculate what the interior looks like with the Radon transform, and it is then possible to produce an image of the interior.

Radon Transform

The Radon Theorem states, that a function $f(x, y)$ is completely defined by a well-defined and absolutely convergent integral p along a line L [27], a condition for the Radon transform is that outside of the function $f(x, y)$ everything has to be zero. The Radon transform is the calculation of $f(x, y)$. To use the Radon transform, the density of the object is measured through different paths from different angles. A projection $p(s)$ is described by the following integral,

$$p(s) = \int_0^s \mu(\eta) \, d\eta,$$

(1)

where η is the coordinate along the path and s the length of the path. μ is the measured density of the whole object in the coordinates of the detector. The coordinates in the rotating system of the detector are (ξ, η), with which the Equation (1) changes to:

$$p_\gamma(\xi) = \int_0^s \mu(\xi, \eta) \, d\eta.$$

(2)

The function $f(x, y)$ is the density function of the object in a fixed coordinate system. To calculate the relation of the two coordinate systems, the unit vectors

$$\vec{n_\xi} = \begin{pmatrix} \cos(\gamma) \\ \sin(\gamma) \end{pmatrix}, \quad \vec{n_\eta} = \begin{pmatrix} -\sin(\gamma) \\ \cos(\gamma) \end{pmatrix}$$

(3)

are defined. Here, γ is the rotation angle of the axis of $\mu(\xi, \eta)$ to $f(x, y)$. Therefore, $f(x, y)$ can be expressed through ξ and η:

$$f(x, y) = \mu(\xi(x, y), \eta(x, y)).$$

(4)
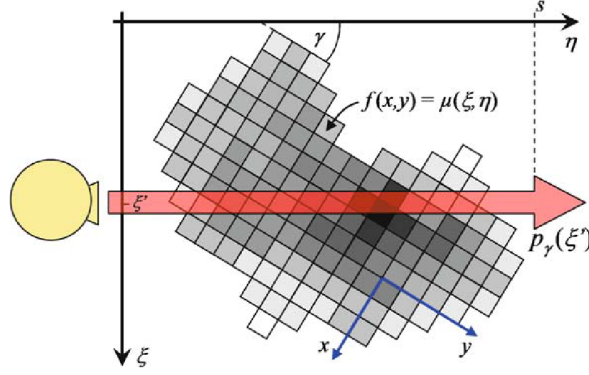
Figure 1: Representation of Radon transform, the detector measures the density of the object. The coordinate system $f(x, y)$ is the system of the object and $p_\gamma(\xi)$ of the detector. The red line represents the projection $p_\gamma(\eta)$. Taken from [8]

With the help of these relations, the path through the object can be expressed with $f(x, y)$. $p_\gamma(\xi)$ is called the Radon transform of the object. By using Equation (4), $p_\gamma(\xi)$ can be expressed as

$$p_\gamma(\xi) = \int\limits_{-\infty}^{\infty} \int\limits_{-\infty}^{\infty} f(x, y)\delta(x\cos(\gamma) + y\sin(\gamma) - \xi)\, dx\, dy. \tag{5}$$

A schematic of the Radon transform is shown in Figure (1), with the different coordinate systems $f(x, y)$ and $\mu(\xi, \eta)$ and the projection $p_\gamma(\eta)$. To illustrate the projection, $p_\gamma(\xi)$ sinograms are used. In a sinogram the value ξ is displayed on the ordinate and the angle γ on the abscissa. The projections are independent of the direction, therefore are all the necessary data of the object acquired with scans from 0°to 180°and only these scans are used in the sinograms.

Inverse Radon Transform and Fourier Slice Theorem

After an experiment the acquired data is usually $p_\gamma(\xi)$ and not $f(x, y)$, therefore the Radon transform is not helpful and the inverse Radon transform is needed. In order to get the distribution $f(x, y)$, the Fourier Slice Theorem (FST) is used, which consists of three steps. The goal of the FST is to calculate the function $f(x, y)$ through using the Fourier transformation for every projection and to apply the inverse Radon transform in the Fourier space. The first step is to use the Fourier transformation in order to calculate $P_\gamma(\xi)$ and $F(u, v)$, which are the Fourier transforms of $p_\gamma(\xi)$ and $f(x, y)$. The important step is the second step, where the Fourier transform of $f(x, y)$ is constructed out of the Fourier transform of $p_\gamma(\xi)$. The third step is to apply the inverse Fourier transformation on $F(u, v)$ to extract $f(x, y)$. The Fourier transform of $p_\gamma(\xi)$ looks like:

$$P_\gamma(q) = \int\limits_{-\infty}^{\infty} p_\gamma(\xi)e^{-2\pi i q\xi}\, d\xi. \tag{6}$$

Equation (1) can be inserted into the formula above, leading to the following equation:

$$P_\gamma(q) = \int\limits_{-\infty}^{\infty} \int\limits_{-\infty}^{\infty} \mu(\xi, \eta)e^{-2\pi i q\xi}\, d\xi\, d\eta. \tag{7}$$

This is the first step of the transformation. The problem between the two Fourier transforms is that they differ in coordinate system. $P_\gamma(q)$ and $p_\gamma(\xi)$ are both expressed in polar coordi-
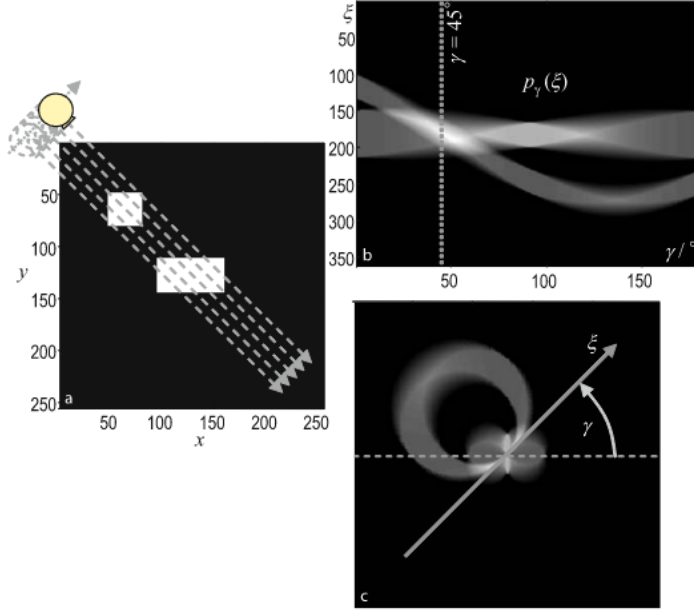
Figure 2: Illustration of the same two objects in different spaces and coordinate systems. **a** Two objects in their coordinate system. **b** Image a in the Cartesian Radon space, after the Radon transform. **c** Image an in a polar Radon space, after the Radon transform. Taken from [8]

nates whereas $F(x, y)$ and $f(x, y)$ are expressed in Cartesian coordinates. The coordinates are transformed from polar coordinates to Cartesian coordinates with

$$u = q \cos \gamma, \quad v = q \sin \gamma. \tag{8}$$

With the help of this substitution, the integral (7) can be expressed as

$$P_\gamma(q) = \int_{-\infty}^{\infty} \int_{-\infty}^{\infty} f(x, y) e^{-2\pi i q (x \cos \gamma + y \sin \gamma)} \, dx \, dy. \tag{9}$$

The 2-dimensional Fourier transform from $f(x, y)$ looks like

$$F(u, v) = \int_{-\infty}^{\infty} \int_{-\infty}^{\infty} f(x, y) e^{-2\pi i (xu + yv)} \, dx \, dy$$
$$= \int_{-\infty}^{\infty} \int_{-\infty}^{\infty} f(x, y) e^{-2\pi i (xq \cos y + yq \sin \gamma)} \, dx \, dy. \tag{10}$$

In the second integral, the substitution from above is used and matches Equation (9). Therefore, $F(u, v)$ in polar coordinates can be defined as

$$F_{\text{polar}}(q, \gamma) = F(q \cos \gamma, q \sin \gamma) = P_\gamma(q). \tag{11}$$

It is the main result of the FST and the basis for Fourier reconstruction. Figure 2 illustrates the different spaces, where the transformation takes place.

Direct Inverse Radon Transform

The direct application of the three steps of the FST and Equation (11) lead to a problem with producing the tomogram. In a measurement, the amount of projections $p_\gamma(\xi)$ is limited. Therefore, also the amount of values in the Fourier transform $F(u, v)$ are limited. The problem is not the amount but the position of these values, because the positions of these values are radially arranged and are not on a Cartesian grid. Due to this problem, the values have to be regridded which means that they have to be defined on a Cartesian grid.

Simple Backprojection

To avoid the problem of regridding, it is possible to use a backprojection process. The thought behind it is that at every object at which the inverse Radon transform was used, it could have been an earlier object in the Radon space which was transformed with the Radon transform. In the Simple Backprojection (SBP), the values are sorted in the polar coordinate system in such a way that the values are ordered like in a Cartesian coordinate system. This is described by the following equation

$$
\begin{aligned}
g(x, y) &= \int_0^\pi p_\gamma(\xi) \, d\gamma \\
&= \int_0^\pi p_\gamma(x \cos \gamma + y \sin \gamma) \, d\gamma.
\end{aligned}
\tag{12}
$$

The problem with this method is that the values are smeared from their original position and the result is a slightly different distribution than originally measured. The projection smears non-negative values on the distribution from the other points of the image grid from the original image. This becomes an even bigger problem for the points outside the object due to the assumption that every point outside the object is zero. If Equation (12), which is supposed to be $f(x, y)$, is inserted in Equation (5), the result is a convolution of the image with the following function:

$$
h(x, y) = \frac{1}{|(x, y)|},
\tag{13}
$$

which is the point-spread function (PSF) of the imaging system. Therefore, every point is smeared with $h(x, y)$ and blurred.

Filtered Backprojection

To solve the problem of the backprojection the change of the coordinate systems is applied in the inverse Fourier transform. The inverse Fourier transform will be performed in polar coordinates. In order to do that, the integration elements du and dv are transformed into $qdqd\gamma$. The q is the result of the Jacobian. The inverse Fourier transform in polar coordinates looks like,

$$
f(x, y) = \int_0^\pi \int_{-\infty}^\infty F(q, \gamma) e^{2\pi i q(x \cos \gamma + y \sin \gamma)} |q| \, dq \, d\gamma.
\tag{14}
$$

Due to symmetries of the Fourier Transform, it is possible to write $|q|$.
The FST (11) is still valid, and because of this, the Hessian normal form can be applied and with

$$
h_\gamma(\xi) = \int_{-\infty}^\infty P_\gamma(q) |q| e^{2\pi i q \xi} \, dq.
\tag{15}
$$
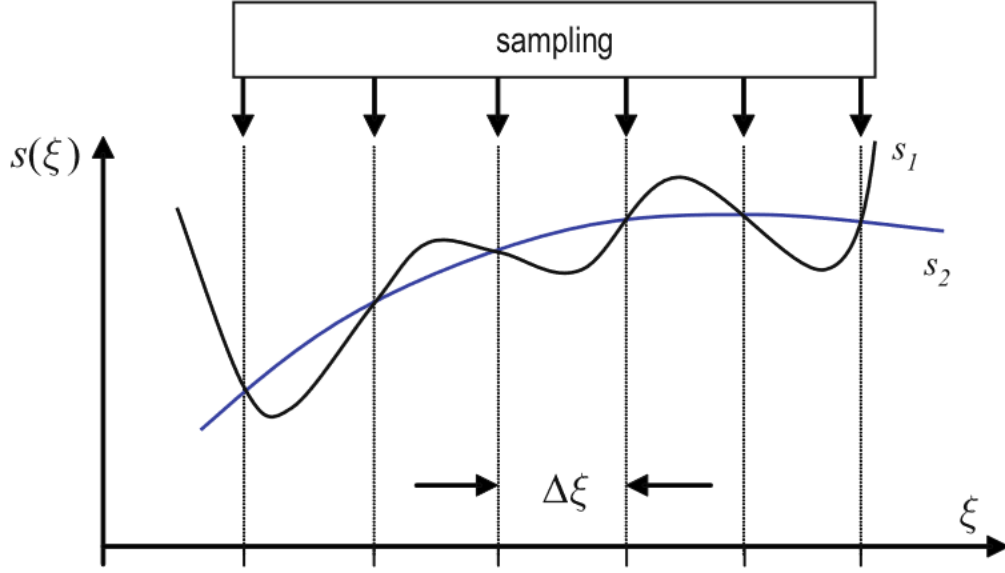
Figure 3: Example of the error of 'aliasing' where different signal functions are described by the same sample points. s_1 and s_2 are interpolation functions of the sample points. $\Delta\xi$ is the step size of the measurement of the signal. Taken from [6]

This allows $f(x, y)$ to be written as

$$f(x, y) = \int_0^\pi h_\gamma(\xi) \, d\gamma. \tag{16}$$

$h_\gamma(\xi)$ is the high-pass filtered projection signal of $p_\gamma(\xi)$ and is therefore called filtered projection. Due to the additional factor $|q|$, $h_\gamma(\xi)$ results to be a high-pass filter. Without this additional factor, it would be $p_\gamma(\xi)$. The difference is that the FBP is in the spectral domain and the direct inverse Radon transform is in the spatial domain. Mathematically, it is the same, but in different domains, and makes a big difference in the reconstruction nonetheless.

Minimum Number of Projections and Pixel

In order to know how many samples are needed to interpolate a signal that represents the measured signal, the Nyquist-Shannon theorem is applied. The Nyquist-Shannon sample theorem says how high the sampling frequency should be to avoid 'aliasing'. 'Aliasing' is the error which occurs when different functions share the same sample points of a signal, $s(\xi)$ which is shown in Figure 3. The Nyquist-Shannon theorem is [26]:

$$f_{\text{sample}} > 2(f_{\text{max}} - f_{\text{min}}). \tag{17}$$

The highest frequency of the measured spectrum is f_{max} and f_{min} is the lowest and f_{sample} is the measuring frequency. The sampling of the signal can be described with the multiplication of a Dirac comb with the signal $s(\xi)$, with the sampling rate η and the number of samples n

$$s_{\text{a}}(\xi) = \sum_{n=-\infty}^{+\infty} s(n\Delta\xi)\delta(\xi - n\Delta\xi). \tag{18}$$

The convolution theorem can be applied on Equation 18 and the sampling $s_a(\xi)$ can be expressed as the Fourier transform $S_a(u)$

6

$$S_{\mathrm{a}}(u) = \frac{1}{\Delta\xi} \sum_{n=-\infty}^{+\infty} \int_{-\infty}^{+\infty} S(v)\delta(u - \frac{n}{\Delta\xi} - v)\, dv. \tag{19}$$

Applying the δ-distribution leads to the final result

$$S_{\mathrm{a}}(u) = \frac{1}{\Delta\xi} \sum_{n=-\infty}^{+\infty} S\left(u - \frac{n}{\Delta\xi}\right). \tag{20}$$

This Fourier transform is the sampled signal of the signal spectrum in the frequency domain. The sampling repeats itself with the period $\frac{1}{\Delta\xi}$. To reconstruct the signal in the frequency domain, an ideal low-pass filter is used with the height of $\Delta\xi$ and multiplied with Equation (20). The convolution theorem will be used once more to gain the reconstructed signal in the spatial domain which is a sinc function

$$s(\xi) = s_{\mathrm{a}}(\xi) * \operatorname{sinc}\left(\frac{\xi}{\Delta\xi}\right). \tag{21}$$

The recovery of the signal is called Shannon-Whittaker interpolation. In the measurement is the period $\Delta\xi$ determined by the number of pixel of the camera or the number of detectors D and the frequency in the spectrum q. $\Delta\xi$ can be calculated by

$$\Delta\xi = \frac{1}{D\Delta q} < \frac{1}{2q_{\mathrm{max}}}, \tag{22}$$

where q_{max} is the maximum available frequency. Δq is directly anti-proportional to the measured field diameter (MFD) [7]. This leads to

$$D_{\mathrm{min}} = 2 * \mathrm{MFD}\, q_{\mathrm{max}}, \tag{23}$$

where D_{min} is the desired number of minimum pixel with the condition of the Nyquist-Shannon theorem. The number of projections is given by

$$N_{\mathrm{P}} = \frac{\pi}{\Delta\gamma}. \tag{24}$$

With the step size of the angles $\Delta\gamma$ can differ between the sample points approximately determined with $0.5\,\mathrm{MFD}\,\Delta\gamma \approx \Delta\xi$. This can be inserted into Equation (24) and this leads to the minimal number of projections

$$N_{\mathrm{P}} \approx \pi \frac{D_{\mathrm{min}}}{2}. \tag{25}$$

2.1.2   Abel transform

The Abel transform generates a 3D-image of the image from of a cross-section. The Abel transform is an algebraic transformation method illustrated in Figure 4. This method is only applicable for distributions with cylindrical symmetry. The result of the Abel transform is a 2D projection of a 3D object. The projection $F(x, z)$ is given by

$$F(x, z) = 2 \int_{x}^{\infty} \frac{f(r, z)r}{\sqrt{r^2 - x^2}}\, dr, \tag{26}$$

where $f(r, z)$ is the 3D distribution of the object in cylindrical coordinates and r is given by $\sqrt{x^2 + y^2}$. The projection $F(x, z)$ is experimentally measurable. With the help of the
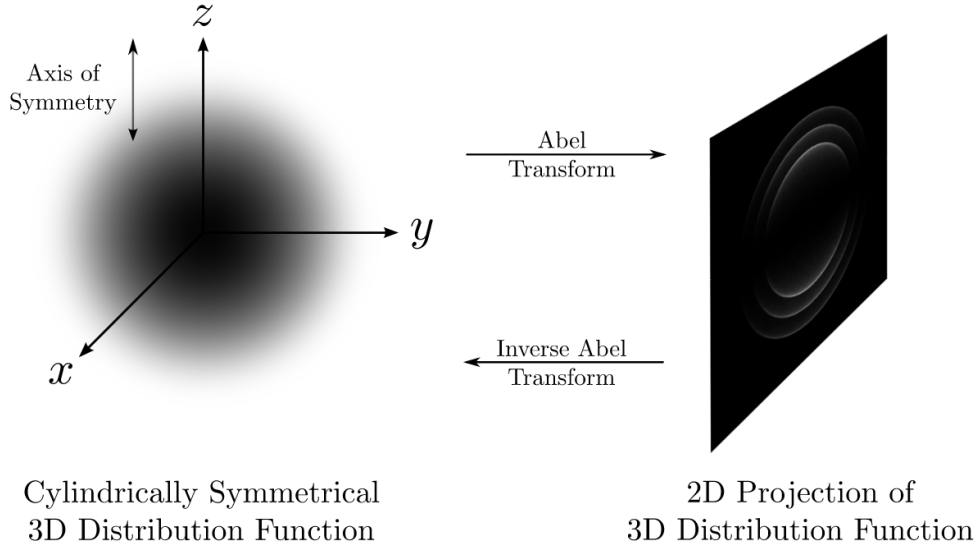
Figure 4: Illustration of the Abel transform. On the left is the object and on the right the Abel transform of the object. Taken from [9]

Inverse Abel transform, it is possible to calculate the 3D distribution only with the single projection $F(x, z)$ with

$$f(r, z) = -\frac{1}{\pi} \int_r^\infty \frac{dF(x, z)}{dx} \frac{1}{\sqrt{x^2 - z^2}} \, dx. \tag{27}$$

The integral limit r is the minimum radius of the projection and therefore also of the reconstructed distribution.

2.2 Photoionization

The photoelectric effect or photoionization is the emission of an electron from an atom due to excitation by radiation. These electrons are called photoelectrons. In order to emit an electron, the light needs to have a certain energy to overcome the ionization energy I_P. The energy of the free electron is described with

$$E = \hbar\omega - I_\mathrm{P}. \tag{28}$$

$\hbar\omega$ is the energy of the photon of the light before the absorption by the electron, where ω is the frequency of the light. The ionization rate Γ depends on the generalized cross-section σ and the intensity I and is described by

$$\Gamma = \sigma I. \tag{29}$$

If the intensity gets too high, these laws can not be applied. In the following, important regimes of the photoelectric effect in a strong laser field are explained.

2.2.1 Keldysh parameter

There are three main regimes how photoionization happens at high intensities of a laser, namely multi-photoionization (MPI), the tunnel effect and the over-the-barrier ionization.

The Keldysh parameter γ indicates how the atom is ionized. MPI occurs for $\gamma \gg 1$, if $\gamma \ll 1$ the electron tunnels over the barrier and if γ is nearly 1 the tunnel effect occurs. The Keldysh parameter describes the ratio between the frequency of the laser ω_{laser} and the inverse time an electron needs to tunnel through a barrier ω_{t} [20]

$$\gamma = \frac{\omega_{\text{laser}}}{\omega_{\text{t}}} = \sqrt{\frac{I_{\text{P}}}{2U_{\text{pond}}}}. \tag{30}$$

γ is proportional to the square root of the ionization energy I_{P} and inverse proportional to the square root of the ponderomotive energy

$$U_{\text{pond}} = \frac{e^2 E^2}{4m_e \omega_{\text{Laser}}^2}. \tag{31}$$

U_{pond} is an additional energy of a free electron in the laser field due to the oscillations of the electromagnetic field of the laser. If the pulse of the laser is long enough, the electron can leave the laser focus and converts the ponderomotive energy into kinetic energy[35].

2.2.2   Multi-photoionization

MPI occurs when the ionization energy I_{P} is much higher compared to U_{pond}. MPI is the ionization with the excitation due to multiple photons. The energies of the photons add up to the ionization energy to emit one electron. This regime depends strongly on the laser intensity I

$$\Gamma_{\text{n}} = \sigma_{\text{n}} I^n, \tag{32}$$

with Γ_{n} the ionization rate and σ_{n} the generalized cross-section for the absorption of photons [16]. n is the minimal number of photons which is needed to ionize the atom. There is a critical intensity I_{S} in this regime, over which the dependence of the intensity changes. Above a certain intensity, no further ionization for a pulse of a given duration occurs, because all the sample atoms have been ionized.

2.2.3   Above-Threshold Ionization

When the atoms absorb more photons than the required n photons to reach I_{P}, the ionization is called Above-Threshold Ionization (ATI). This is only possible as long the ejected electron is still in the Coulomb field of the atom due to the laws of energy and momentum conversation

$$\Gamma_{n+s} \propto I^{n+s}. \tag{33}$$

Due to this effect, the Equation (28) changes to

$$E = (n + s)\hbar\omega - I_{\text{P}}, \tag{34}$$

where s is the number of additional absorbed photons [17]. The photoelectron spectrum (PES) has peaks at multiples of $\hbar\omega$ and the energy of the peaks is given by Equation (34). The number and intensity of the peaks depend on the intensity of the laser. After the ionization, the initial direction of the photoelectrons is aligned with the polarization of the laser[18].

2.2.4   AC stark shifts

The atomic states shift with the laser field. The higher the intensity of the laser, the stronger are the shifts. These shifts are called AC Stark shifts. The AC Stark shifts are visible on the PES, some peaks can be missing and others don't follow the Equation 34. Figure 5 shows the impact of the AC Stark shifts in measurement with different intensities.
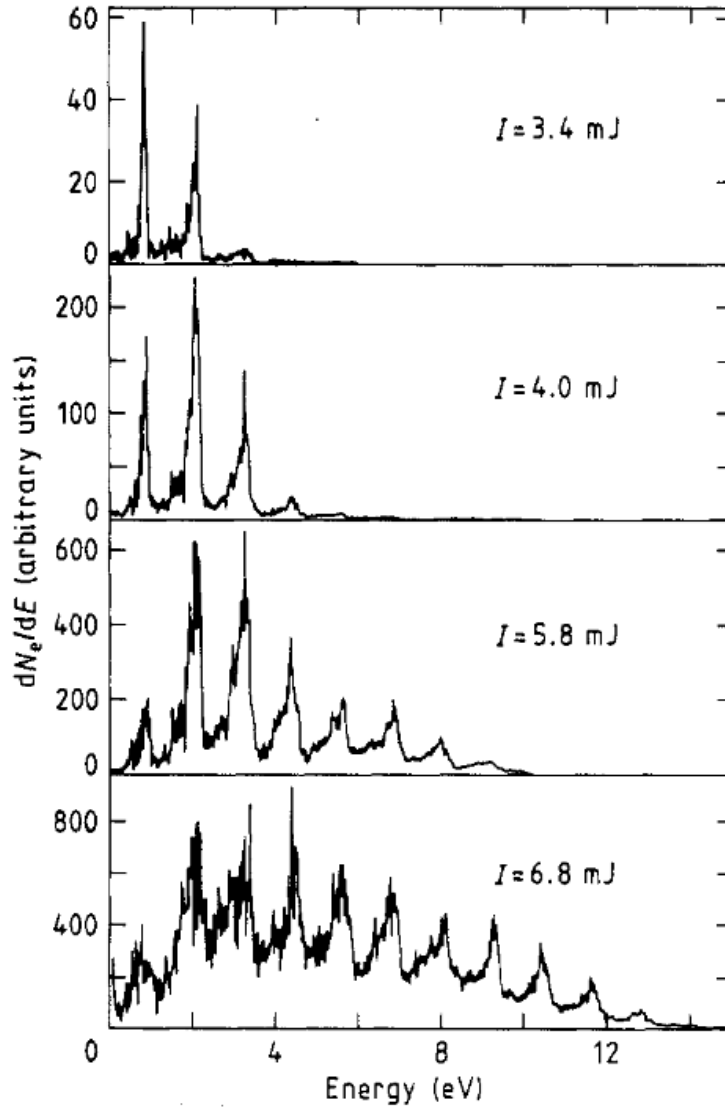
Figure 5: Measurements of different spectra with different pulse energies for a pulse duration of 135 ps. The increasing peaks and the broadening of the peaks show the AC Stark shifts. The first peak disappears at around 7 mJ, due to channel closing. Taken from [34]

Channel closing

The energy of free electrons in a laser field is U_{P}. If the laser intensity is high enough, U_{P} also has an impact on the bound electrons. The atomic states of the weakly bound electrons shift due to the AC Stark effect with an energy close to U_{P}. The shifts of the low states near the nucleus can be neglected. Therefore, the ionization potential increases with U_{P}. The required energy for the ionization is

$$I_{\mathrm{P}} + U_{\mathrm{P}} = \hbar\omega k, \tag{35}$$

with the integer k. The channel k is closed when k photons are no longer sufficient and $k+1$ photons are needed to ionize the atom. Because of channel closing, the first peaks on the PES are suppressed [21]. The Equation (34) changes to

$$E = (n + s)\hbar\omega - (I_P + U_{\mathrm{pond}}) \tag{36}$$

Channel switching

The ionization potential of excited weakly bound states shifts upward. Due to this shift, these levels resonate with a harmonic of the laser field at some intensity. This leads to an enhancement of the ionization rate of the bound states, thus the PES shows peaks of excited bound states [17].

2.2.5 Tunnel ionization

When γ is much smaller than 1, the electrons can tunnel ionize. When the ionization potential is low compared to the intensity, γ is much smaller than 1. The field of the laser effects the atomic potential in a way that tunnel ionization is possible.

High-Harmonic Generations

In a semi-classical approach, the electron is viewed as a wave package. As explained, the atomic potential is affected by the field of the laser. This happens within one circulation of the field. The electron tunnels through the barrier. As the field of the laser changes, the electron 'falls' back into the potential and due to this fall releases a photon. The photon has the combined energy of the ionization potential and the former kinetic energy of the electron. As shown in Figure 6.

Over the barrier ionization

The higher the intensity, the stronger the atomic potential is modified by the light field. At some point the intensity is that high that the barrier is too small, and the ground state becomes free, which allows the electron to leave the potential. This is called over the barrier ionization (OBI).

## 2.3 Femtosecond enhancement cavity

In the experiment, the laser is enhanced in an optical enhancement cavity. The used laser is a frequency comb. The theory behind this cavity and the laser is explained in this subchapter.

2.3.1 Optical resonators

In a cavity, the light of the laser resonates. The light or the electric field E of a continous-wave laser can be described by a wave

$$E(\vec{x}, t) = E_0 e^{\omega_0 t - \vec{k}\vec{x}}, \tag{37}$$
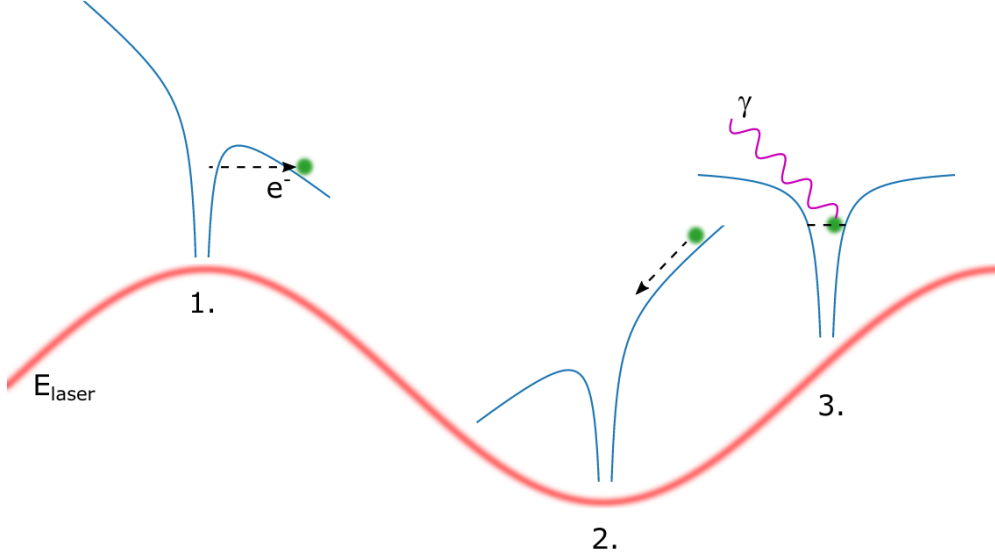
Figure 6: The three step model. The electron gets lifted over the potential barrier (1.), the laser field oscillates and the electron falls back in the potential well(2.) and releases a photon(3.). Taken from [24]

where t is the time, $\vec{k}$ is the wave vector, E_0 the field amplitude, ω the angular frequency of the wave and $\vec{x}$ the location vector. To build a resonator, mirrors are used. One of these mirrors is an Input Coupler (IC). This means that this mirror has a transmission t_{IC} which is not negligible. This allows that light to pass through this mirror into the cavity. Because the light resonates, multiple waves superimpose in the resonator. The field of the waves is in an equilibrium, it can be described as

$$E_c(\omega) = E_{\text{in}} t_{\text{ic}} \sum_n (r_{\text{ic}} r_c e^{i\phi(\omega)})^n. \tag{38}$$

r_{IC} is the reflectivity of the IC, r_c is the reflectivity of the cavity, ϕ is the phase of the wave, and E_{in} the field of the laser which gets into the cavity through the IC. The equilibrium converges to

$$E_c(\omega) = \frac{E_{\text{in}} t_{\text{ic}}}{1 - r_{\text{ic}} r_c e^{i\phi(\omega)}}, \tag{39}$$

because both reflectivity values are below 1. ϕ is defined by

$$\phi(\omega) = \frac{\omega L}{c} + \phi_{\text{d}}(\omega). \tag{40}$$

ϕ_d is the shift produced by possible diversion at the mirrors, which will be neglected in the following. E_C is at its maximum when

$$\frac{\omega L}{c} = 2\pi n, \tag{41}$$

which is the condition for resonance. n can be any integer and L is the length of the resonator [24].

The enhancement of the resonator is defined by the ratio of the intensity of the incoming light I_{IC} through the IC and the intensity of the resonating light I_C within the cavity

$$\beta = \frac{I_c}{I_{\text{in}}} = \frac{|E_c|^2}{|E_{\text{in}}|^2} = \frac{t_{\text{ic}}^2}{(1 - r_{\text{ic}} r_c)^2}. \tag{42}$$

12

The electric field which resonates and gets reflected in the cavity can be determined with

$$E_{\text{ref}}(\omega) = E_{\text{in}} \frac{r_c t_{\text{ic}}^2 e^{i\phi(\omega) - r_{\text{ic}}}}{1 - r_{\text{ic}} r_c t_{\text{ic}}^2 e^{i\phi(\omega)}} \tag{43}$$

Polarization in an optical resonator

In principle the reflectivity, and thus the enhancement in a cavity, can be dependent on the light polarization. Polarization is the direction of the vector of the electric field $\vec{E}$. The polarization of a laser can be linear. Linear polarization can be described by a constant direction of polarization, but the absolute value and the algebraic sign of E vary. This way, $\vec{E} = \vec{E}_x + \vec{E}_y$ is constant and $\vec{E}_x$ and $\vec{E}_y$ are in phase [12]. To calculate whether the resonator is polarization sensitive, the following equation can be used:

$$\frac{\beta}{C} = \frac{1}{\epsilon t_c^2}, \tag{44}$$

C is the cavity contrast, β the enhancement of the resonator, t_C the transmissivity of the mirrors in the cavity and ϵ is the mode matching factor. The cavity contrast is the ratio of the decrease of the reflected intensity and I_{in}. The bigger C is, the more light gets coupled into the resonator. It is defined by

$$C = \frac{I_{\text{in}} - I_{\text{ref,tot}}}{I_{\text{in}}}, \tag{45}$$

where $I_{\text{ref,tot}}$ is the total reflected intensity in the cavity. The mode matching factor indicates how well the mode of the cavity matches the incoming light at the position of the input coupler.

With ϵ, the intensity of the incoming beam I_{in} and the reflected intensity I_{ref}, the total intensity $I_{\text{ref,tot}}$ can be calculated

$$I_{\text{ref,tot}} = \epsilon I_{\text{ref}} + (1 - \epsilon) I_{\text{in}}. \tag{46}$$

The ratio of β and C depends only on the transmissivity, $T_C = t_C^2$ and ϵ therefore it should stay constant for changing polarization with polarization independent mirrors. If the ratio is constant but β changes, another cause has to be considered.

2.3.2 Frequency comb

The frequency comb (FC) is a powerful tool to determine unknown frequencies, when it was developed in 1998 it measured frequencies up to $1\,\text{THz}$[32]. The spectrum of the frequency comb is defined by two frequencies. The carrier-envelope-offset frequency f_{CEO} shows the offset of the comb from zero. The repetition frequency f_{rep} is the gap frequency between two modes. The spectrum of the FC is described with

$$f_n = f_{\text{CEO}} + n f_{\text{rep}}. \tag{47}$$

This formula shows the frequency of the nth mode. Overall, there are about 10^5 modes in one envelope. f_{rep} is described by the time gap between two consecutive pulses T_{rep}

$$f_{\text{rep}} = \frac{1}{T_{\text{rep}}}. \tag{48}$$

f_{CEO} can be calculated with T_{rep} and the carrier phase difference between consecutive pulses $\Delta\phi_{\text{CEO}}$ [25]

$$f_{\text{CEO}} = \frac{\Delta\phi_{\text{CEO}}}{2\pi T_{\text{rep}}}. \tag{49}$$

The intensity of the beam is only non-zero for $\omega T_{\text{rep}} + \Delta\phi_{\text{CEO}} = n2\pi$. A frequency comb is illustrated in Figure 7 in two plots, in the upper plot are the pulses of a frequency comb shown and in the plot above one envelope of a frequency comb with its modes.

13
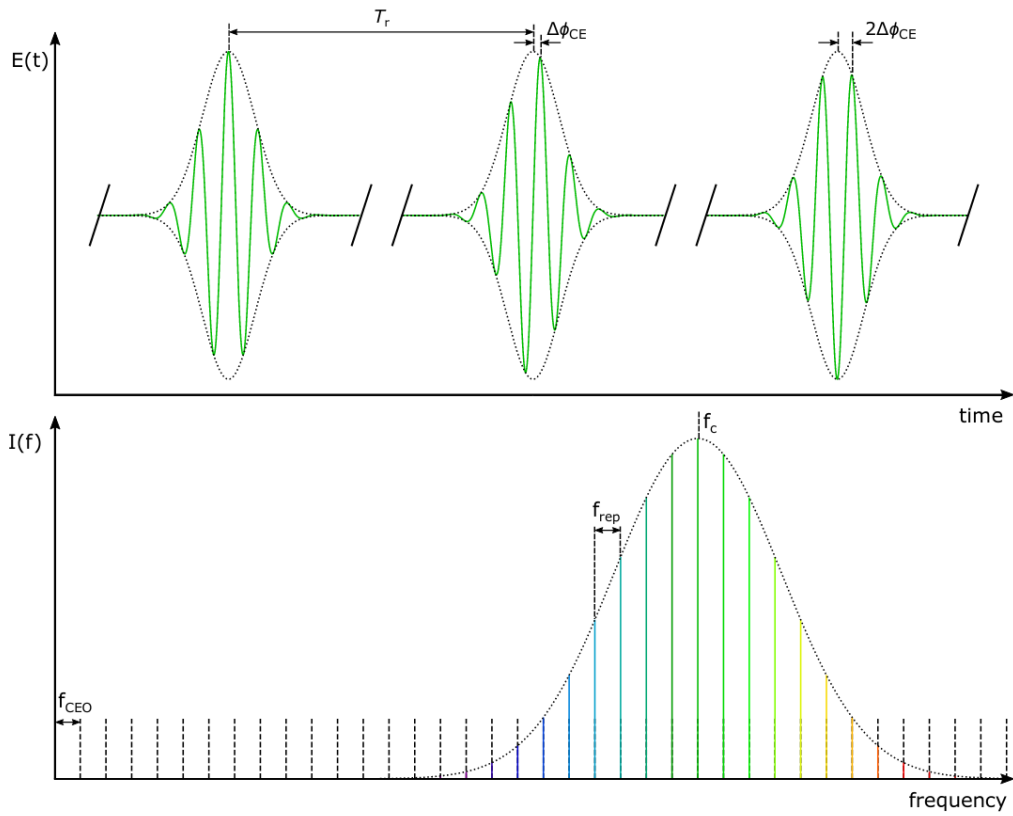
Figure 7: The frequency comb. The upper plot shows the pulses of a frequency comb with the time gap T_r and the carrier-to-envelope phase $\Delta\phi_{CE}$, the plot below shows one envelope of the frequency comb with the characteristic frequencies f_{rep} and f_{CEO}. Taken from [24]

2.3.3 Femtosecond enhancement Cavity

In chapter 2.3.1, it was described how continous-wave light resonates in a resonator. To enhance a pulsed laser beam, several more conditions to the resonator are added. The gap between two consecutive resonances in a resonator is defined by Equation (41). This gap has to fulfill the condition $L = n\lambda$ and it is called free spectral range

$$\Delta\omega_{\mathrm{FSR}} = \frac{2\pi c}{L}. \tag{50}$$

One condition that has to be fulfilled to enhance femtosecond (fs) pulses is, that the modes from the FC have to be simultaneously resonant with the cavity. This means that

$$\omega_{\mathrm{rep}} = n\Delta\omega_{\mathrm{FSR}} \tag{51}$$

has to apply for the cavity.

Furthermore, all the pulses have to overlap coherently with the other pulses, which is described by

$$T_{\mathrm{rep}}c = nL, \tag{52}$$

with n being an integer and T_{rep} the repetition time of the pulses. With these two conditions, the ideal length of the cavity can be calculated

$$L = \frac{c}{f_{\mathrm{rep}}}, \tag{53}$$

which maximizes the enhancement. For a dispersionless cavity, the third condition is,

$$\Delta f_{\mathrm{CEO}} = 0. \tag{54}$$

This allows constructive interference between the circulating pulse and an incoming pulse. These three conditions define an ideal femtosecond enhancement cavity.

3 Experimental setup

In this chapter, the experimental setup will be explained. The setup consists of the laser system, the cavity, and the Velocity Map Imaging setup. First, an overview of the laser system with the frequency comb and the optics setup will be given. In the next section, the enhancement cavity will be described, followed by an explanation of the VMI setup.

3.1 Laser system

The laser is a commercial frequency comb (Menlo Systems, FC1000-250) with the repetition rate of $100\,\text{MHz}$. The spectral bandwidth is $14\,\text{nm}$ FWHM and is centered around $1039\,\text{nm}$. The laser has a power of $10\,\text{W}$ and it is possible to amplify the laser up to $70\,\text{W}$. The beam geometry of the laser inside the UHV chamber and the cavity are illustrated in Figure 8. The cavity is in an ultra-high vacuum (UHV) chamber. In front of the UHV chamber, there is a $\frac{\lambda}{2}$-wave plate to change the polarization of the laser. The mode of the laser is matched in front of the UHV chamber and f_{ceo} is set at the laser. Inside the UHV chamber, the laser beam is coupled into the cavity.

3.2 Cavity

The resonance length of the cavity is as long as the distance of two laser pulses, which is $3\,\text{m}$. The cavity consists of six mirrors, as it is shown in Figure 8 and in Figure 9, where the mirrors more explained in detail in the caption. The beam enters the cavity through the input coupler (IC), the first mirror. The IC has a transmissivity which is not negligible. The transmitted light is directed to a photodiode, which is shown in Figure 8, where the power of the light is proportional to the power in the cavity. During the measurement was the intensity in the focus of the cavity $6.05 \times 10^{12}\,\text{W}\,\text{cm}^{-2}$. With the intensity inside the cavity, it is possible to calculate the enhancement β after a calibration. Between the two spherical concave mirrors 5 and 6, the beam is focused (9). The mirrors number 2, 3, and 4 are plane mirrors. Moreover, the length of the cavity is adjustable, due to a piezo element on which the third mirror is glued. If a voltage is applied is to a piezo element, it expands or contracts depending on the polarity of the voltage. With the help of the piezo element, it is possible to change the length of the cavity by nanometers to stay on the resonance length. In order to do that, the piezo element is applied to a periodic voltage which is scanned. With the help of the measured power, the voltage can be adjusted so that the length of the cavity stays nearly equal to the resonance length and to calculate the cavity contrast C. The mirror glued on the piezo element is also mounted on a stage which is movable to correct in bigger steps. With this, it is possible to change the length of the cavity up to $1\,\text{cm}$. This
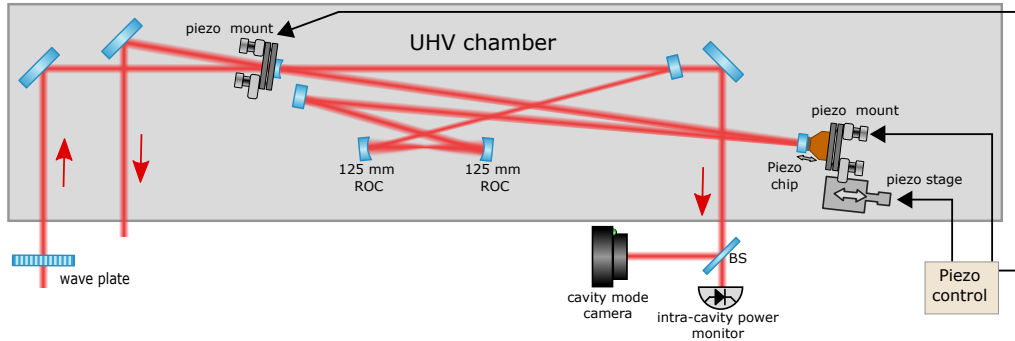
Figure 8: The ultra-high vacuum chamber (in gray) with the cavity inside. Outside the UHV chamber is only the wave plate, the photodiode for measuring the intracavity power and the piezo control. The red lines illustrate the laser.
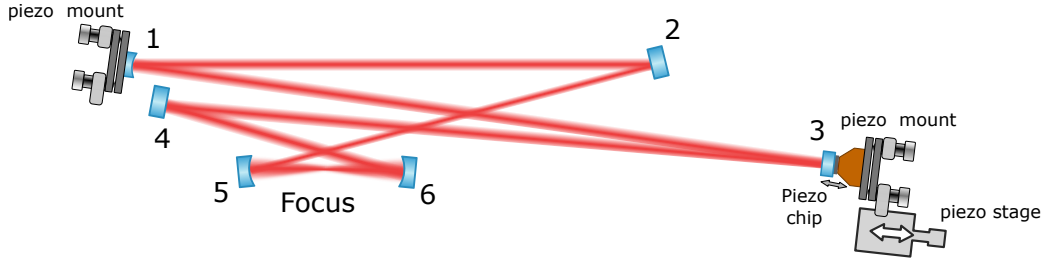
Figure 9: Illustration of the cavity. 1 is the Input Coupler, the light enters through the IC into the cavity. It is mounted on a piezo mount. 2, 3 and 4 are plane mirrors. 3 is glued on a piezo element and mounted on an adjustable piezo stage. 5 and 6 are concave mirrors. The laser beam is focused between mirror 5 and 6.

is the first method to keep the resonance length of the cavity. The second method is the Pound-Drever-Hall laser frequency stabilization, where the derivative of the intensity of the reflected beam is measured. Due to changes of the frequency of the laser, the intensity inside the cavity changes. The derivative of the intensity shows whether the frequency is above or below the resonant frequency of the cavity. With the help of the feedback, the frequency is adjusted and the cavity is 'locked' on the resonance length [10]. In the measurement was the Pound-Drever-Hall method used. For the measurement, it is necessary that the cavity stays in resonance in order to have a constant intensity for the ionization, due to Equation (32). Therefore, it is important that the mirrors in the cavity are polarization independent. The incoming beam is reflected at a mirror, where also light is transmitted. This light is led to a beam splitter in order to measure the intensity in the cavity and to see the mode of the beam with a camera. The mode of the beam can be adjusted if needed with the change of the length of the cavity via the piezo element.

3.3 Velocity Map Imaging

3.3.1 Velocity Map Imaging

Velocity Map Imaging (VMI) is an ion imaging method developed by Eppink and Parker in 1997. It is an improvement in the area of Photofragment-ion imaging or Product Imaging developed by Houston and Chandler in 1987 ([11]). The goal of Product Imaging is to measure the internal energy and the velocity simultaneously. In Product Imaging, atoms or molecules are ionized with a laser. The electrons are directed onto an imaging detector with the help of a repeller and a homogeneous extraction field generated by two grounded grids. The detector is a microchannel plate (MCP) with a phosphor screen. The MCP is an electron multiplier, which consists of two electrodes and an array of glass channels. A voltage is applied on the electrodes in a way that they produce a parallel electric field. Secondary electrons are generated in the glass channels when ionizing radiation or particles impinges on the input of the array, therefore the electrons are multiplied and these electrons are detected[28]. The velocity of the electrons is obtained by the position on the phosphor screen, and the obtained distribution is 2D. It is possible to generate the 3D distribution by applying the Abel transform, and the ion distribution has to be cylinder symmetrical ([11]). With the original method, one of the problems was the resolution of the image due to the width of the polarizing laser and therefore a wide line of electrons. This wide line produced a blurring on the detector. Additionally, the grids decreased the transmission of the electrons and caused distortions on the image [29]. To avoid the blurring, Eppink and Parker developed electrode lenses to 'deblurr' or focus the electrons on the detector. They replaced the grids with ring shaped electrodes. Due to the ring shaped electrodes, the electrons are sorted on the detector according to the velocity independent of the place of
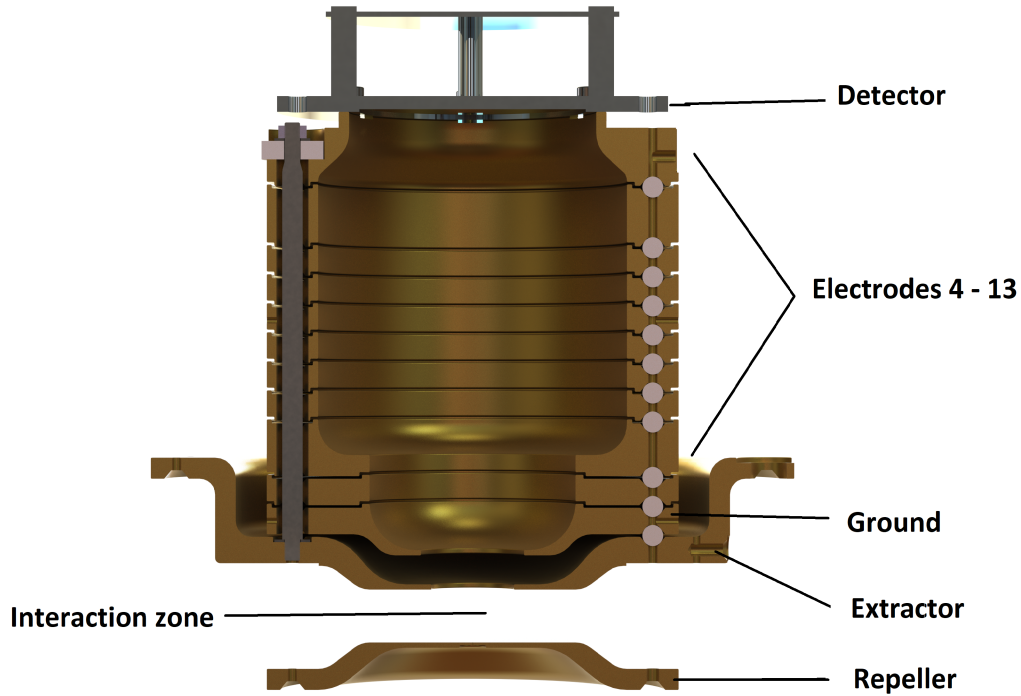
Figure 10: Illustration of the VMI. At the bottom is the repeller electrode. Between the repeller and the extractor, the atoms are ionized in the interaction zone. Above the extractor is the ground electrode. Small balls and bars hold electrodes 4 to 13 in space, which shield the inner TOF tube. At the top is the MCP detector with a phosphor screen.

ionization, which improved the resolution. The Velocity Map Imaging setup consists mainly out of three electrodes and the MCP. The electrodes function as a lens. With the voltage ratio of the repeller and the extractor electrode, the electrons are focused on the detector independent of the length of the time-of-flight (TOF) tube. The right setting for the ratio has to be determined for each setup, either through experiments or with simulations. The total voltages determine the spread of the electrons on the detector. The third electrode is the ground to prevent the extraction field reaching in the TOF tube. Another effect of the ring shaped electrodes is that the transmission reaches 100% and there are no more distortions caused by grids [15]. The VMI method does not only function for electrons, but also for ions and in general with electrically charged particles.

VMI works ideally when these three requirements, formulated by Eppink and Parker, are met:

1. The distributions of the ions should collapse along the axis of the TOF tube so that the spread of the TOF of the different particles is minimal.

2. The image size has to be linearly proportional to the expansion speed for every kinetic energy release.

3. The location of the ionization should be as small as possible to reduce the errors due to the shape or propagation of the laser beam.

3.4 Velocity Map Imaging Setup

The used VMI setup follows the example of the setup of Eppink and Parker. In Figure 10 the structure of the VMI is illustrated. It is located in the focus of the cavity. The setup

is symmetrical in the axis of the detector. It has a height of 130 mm and a diameter of 125 mm. The gas target is injected through a nozzle in a small hole of 100 µm in the repeller electrode. It is injected along the rotation axis, to which the laser is orthogonal. The setup consists of several electrodes. The three electrodes at the bottom are the repeller, extractor and the ground electrode like in the setup of Eppink and Parker. The voltage ratio between the extractor electrode to the repeller electrode is 0.738 ± 0.001 [33], to have the optimal focus on the detector. The purpose of the upper electrodes is to protect the TOF tube from other interfering fields and manipulate the expanding distributions in other experiments, in instance with additional lenses. To protect the TOF tube effectively, the electrodes overlap each other. The electrodes are held in position by three small balls and three bars. The last electrode is the MCP- detector[3]. The MCP- detector is 110 mm above the interaction region and has a diameter of 44 mm. The channels of the detector have a diameter of 12 µm. The phosphor screen is integrated into the MCP.

A camera [1] is pointed to the phosphor screen. The camera, with all the settings for exposure time and gain, is controlled from a computer. With the help of a python program, the images are taken and saved. This also allows controlling the data acquisition live in order to respond to fluctuations of the intracavity power.

4 Data evaluation

In this chapter, the measured data of ATI of xenon is shown and analyzed. There have been two measurements, the first was over 36 different angles and the second over 90 different angles of polarization. At the second measurement, the intracavity power was kept constant by adjusting the input power, due to the higher number of angles, the data of the second measurement was used. The polarization angle was changed in steps of 2°, the first measured angle was 52°away from s-polarization, therefore at the 26st measured angle was the laser s-polarized. The last measured angle was 36°away from p-polarization. On the images is the velocity vector of the photoelectrons shown, thus represents the radial location of a pixel the velocity of photoelectrons. At first, the captured images are shown, and it is explained how the image were configured. In the second subchapter are the data evaluated, which the images provide, and in the last part of this chapter the reconstruction methods are compared and applied on the images.

## 4.1 Data processing and artifact correction

In order to use the images in the intended way, the images have to be processed. In a self written python program [5], the images are cropped and the background is subtracted. For each angle of the electron momentum distribution or polarization, several images are taken. The images are superimposed and divided by the number of images per angle to get the average intensity of each pixel. On the original images, several pixels have bright spots which are on the basis of the VMI and not of the electron resolution. These bright spots are on the same pixel even though the polarization changes and the brightness of the spots is dependent on the brightness of the electron momentum distribution, which leads to the assumption that some micro channels of the MCP are defect and release more electrons, which results in a stronger signal on the phosphor screen. In the python program, these bright spots are detected and corrected. In order to correct them and without changing more than necessary, the bright spots are replaced with a least-square-fit of the immediate environment of the bright spot. The environment around the bright spot is not changed in the process. This correction is applied on all the bright spots on all the images. These edited images are saved for the further reconstruction of the electron momentum distribution.

4.2 Characterization of the data

4.2.1 Intensity of the images

In order to extract information from the images, plots of the integrated intensity over the angle are calculated. In Figure 13 selected plots of the intensity over the radius are shown. The peaks represent the rings of the electron momentum distribution. The second and third peaks are recognizable on all the images, the first peak disappears for the angles from the 26th angle to the 41st angle. A reason for this could be the polarization, because at the 26th angle, the laser beam is s-polarized. Hence, the rings are above each other and transition from one ring to another are more fluid on display. Another reason is that the laser intensity inside the cavity and of the measurement of the angles is unstable. The intensity of the whole original image over the measured angle is shown in Figure 14. In the range where the first peak is not recognizable in Figure 13, a minimum of the intensity is noticeable in Figure 14. Due to this changing intensity of the images, the intensity of all images was normalized to the minimum intensity value. The intensity should be constant, because the difference between the polarization angles is not the amount of ionized electrons, but the velocity vector of the ionized electrons.

The power inside the cavity was recorded during the whole measurement for each polarization angle with the help of a photodiode. These recorded traces of the intensity inside the cavity are shown in Figure 15, where the intensity is plotted over the polarization angle. The maximum intensity inside the cavity stays nearly the same all the time, but the mean
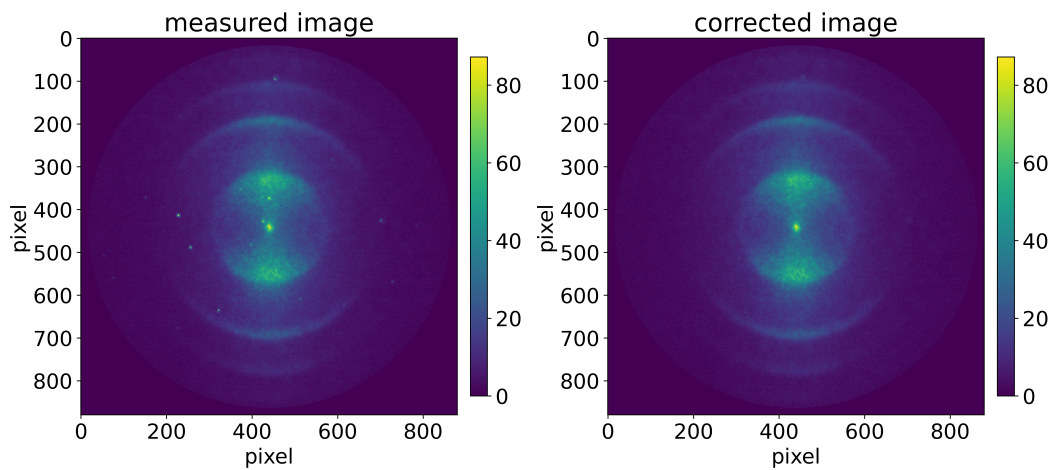
Figure 11: On the left is an example of a measured image of the ATI of xenon with the punctual artifacts. On the right is the corrected image where all the artifacts have been removed. The angle of this image is 52°away from the s-polarization. It is the first measured angle.
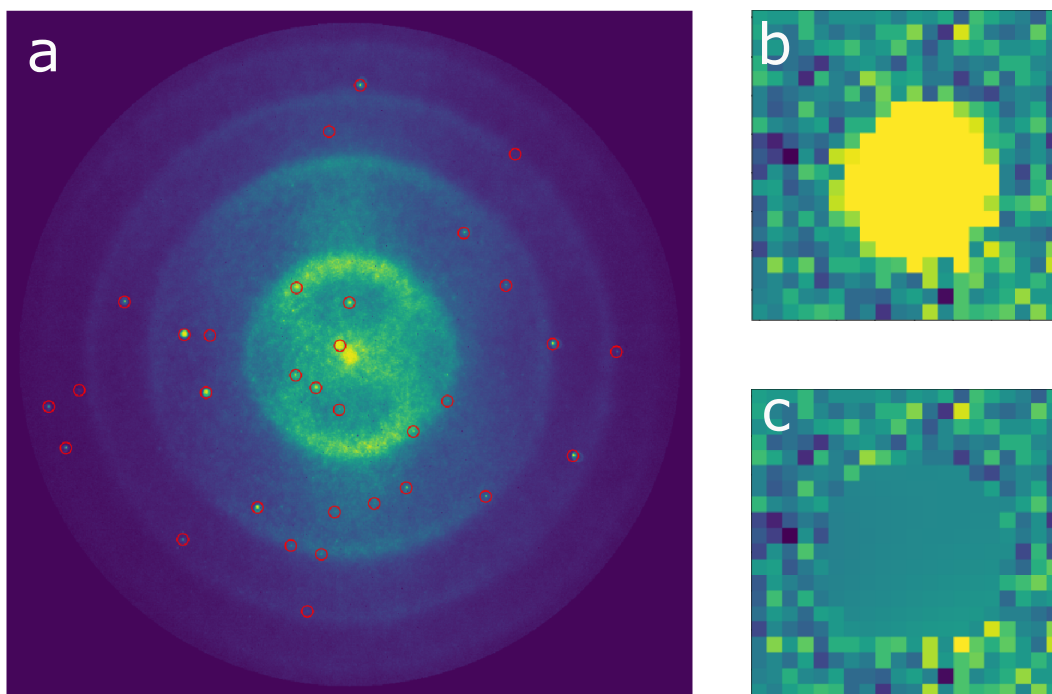
Figure 12: a Raw image of the ATI photoelectron spectrum with laser polarization 48°away from s-polarization with artifacts marked in red circles. It is the second measured image. b Enlarged artifact from the measured image. c the corrected artifact, it is the same as in b.
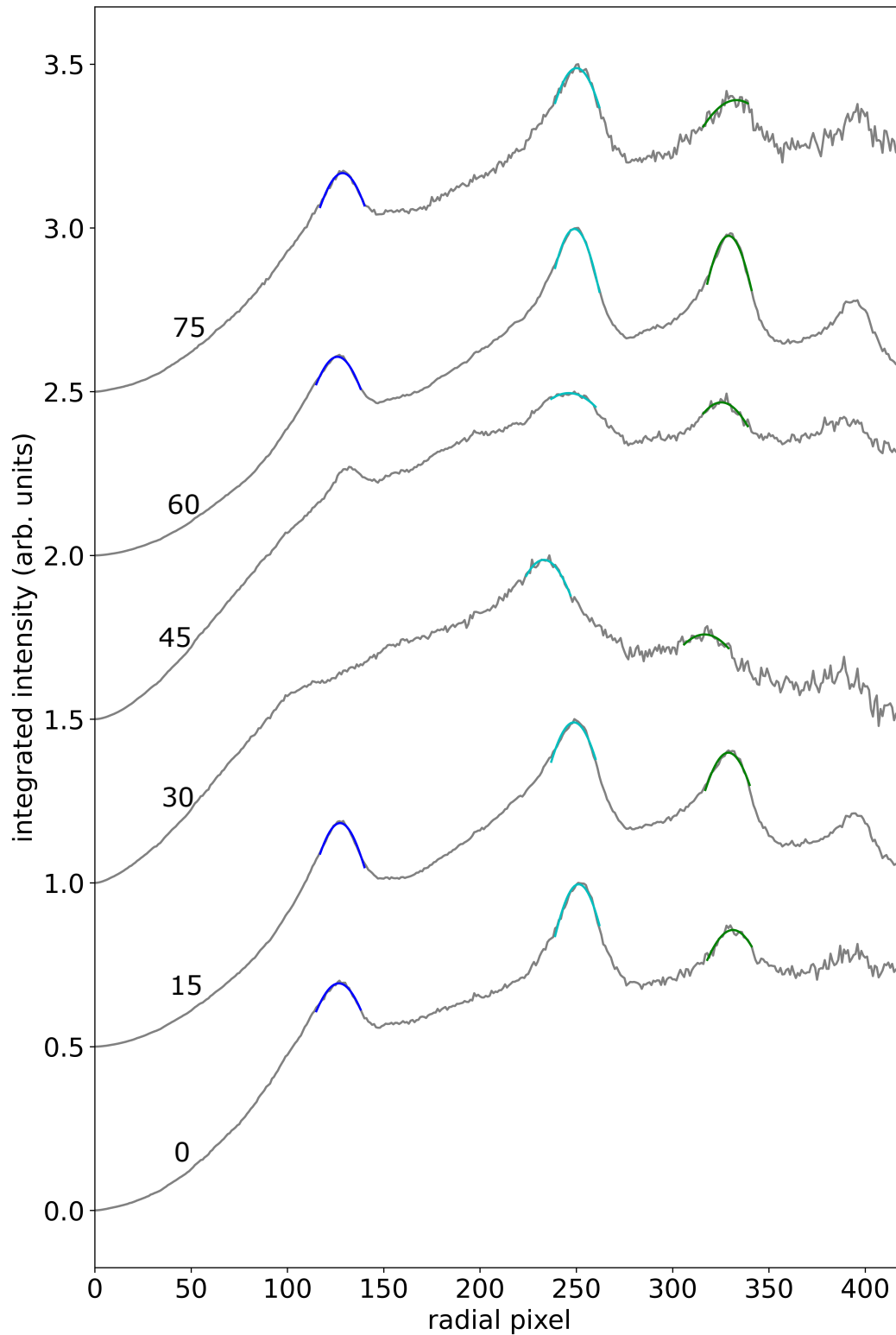
Figure 13: The integrated intensity plotted over the radius representing the angle-independent photoelectron velocity spectrum for different polarization angles. The peaks are fitted with a Gaussian, the first peak is fitted in blue, the second in cyan and the third in green. In the range between the 24 and the 48 measured angle was no Gaussian fitted to the first peak. The number over each plot represents the measured angle, between each measured angle is a step of 2°polarization. The intensities are fitted with an increasing offset.

22
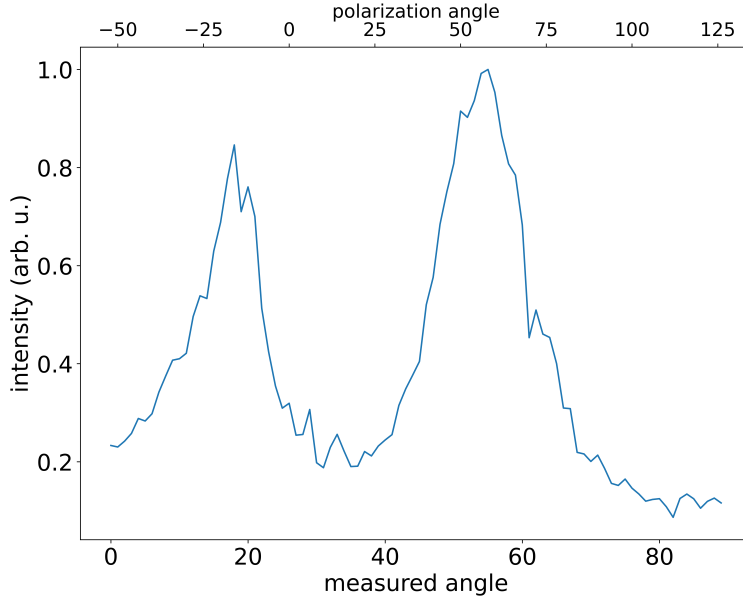
Figure 14: This figure shows the total intensity of each image over the measured angles. The s-polarization of the laser is the 26th measured angle, where the polarization angle is 0, and the p-polarization is the 71th measured angle. Because a $\frac{\lambda}{2}$-wave plate was used, is the step size between two measured angles $2°$of the polarization angle.

intensity drops in the same range of polarization angles as the total intensity of the measured images has a minimum. The standard deviation of the traces also increases by the same amount for the remaining polarization angles when the intensity drops. Because of these two reasons, it is possible that the first peak is not visible in the plots of the integrated intensity. In order to determine the peak width, the identifiable peaks in the plots are fitted with a Gaussian. The peak widths of the second and third peaks are plotted in Figure 16. In the range from the 20th to the 60st measured angle the second peaks are broader than for the other measured angles, and the width of the third peaks is increased in this range from the 25th to the 45th angle compared to the average width of the third peak. This leads to the conclusion that the fluctuation of the intensity inside the cavity affects the peaks and the whole radial intensity spectrum of the measurements. The fluctuations in the intensity plots in Figure (13) increase as the radius increases. Therefore, it is more difficult to fit the Gaussian on the peaks and because of this, there are more fluctuations in width of the third peak. Especially for higher angles, fluctuations increase.

4.2.2 Energy calibration

The location of the electron rings corresponds to their momentum and is thus energy dependent. The energy depends quadratically on the velocity of the electrons and therefore also on the radial location of the electrons in the images, with

$$E(r) = ar^2 + c = s\hbar\omega, \tag{55}$$

where c is the energy offset and s the number of photons above the required n for ATI, as in Equation (34). Which leads to the following equation

$$c = (n + s)\hbar\omega - (I_{\text{P}} + ar^2 + U_{\text{pond}}). \tag{56}$$

With the help of the location of the peaks, it is possible to calculate the ponderomotive shift. In order to do this, a fit was made for each projection using the Equation (55). The energy
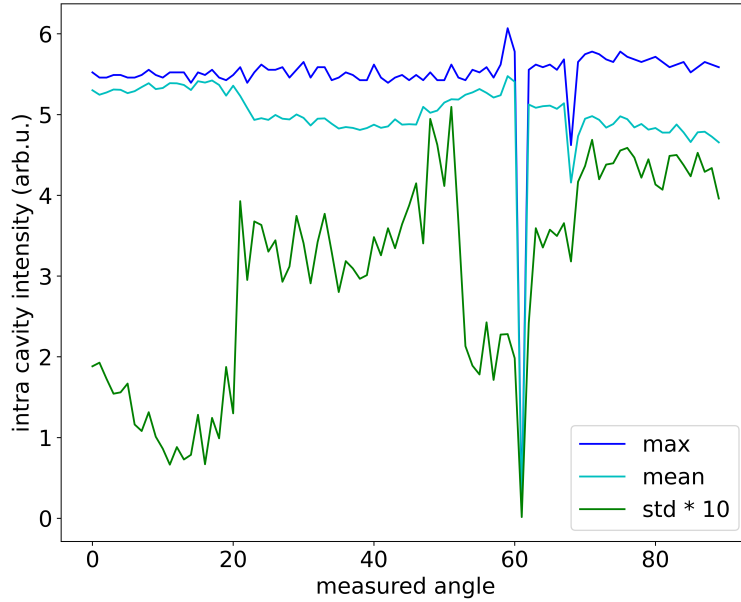
Figure 15: The measured intracavity power over the measured angles. It was measured with a photodiode for a period of 100 ms. The blue line shows the maximum intensity, the cyan line is the mean intensity, and the green line shows the standard deviation. In the range between measured angle 20 and 45 dropped the mean intracavity power, which is a reason for the drop of the intensity in Figure 14.
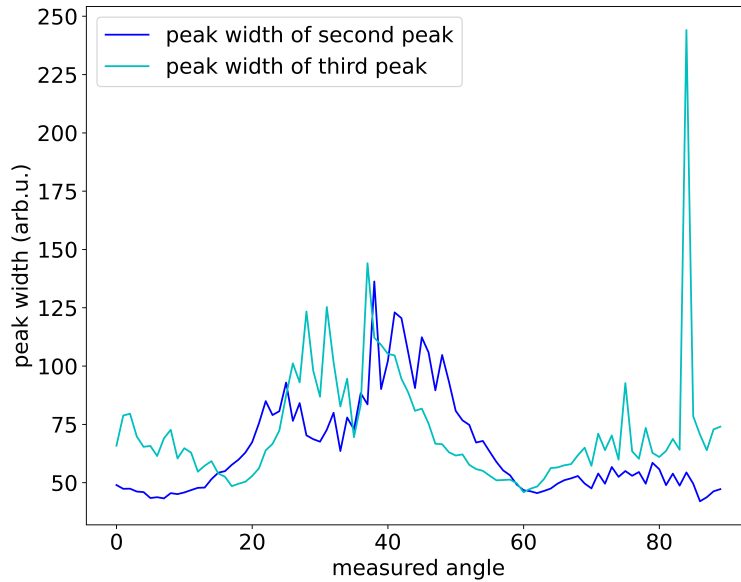
Figure 16: The FWHM of the peaks of the Gaussian fits from Figure 13. The first peak is not plotted, due to its missing in the range of the 24st to the 48st measured angles. In the same range is the FWHM of the second and the third peaks wider than before and fluctuates more.

24
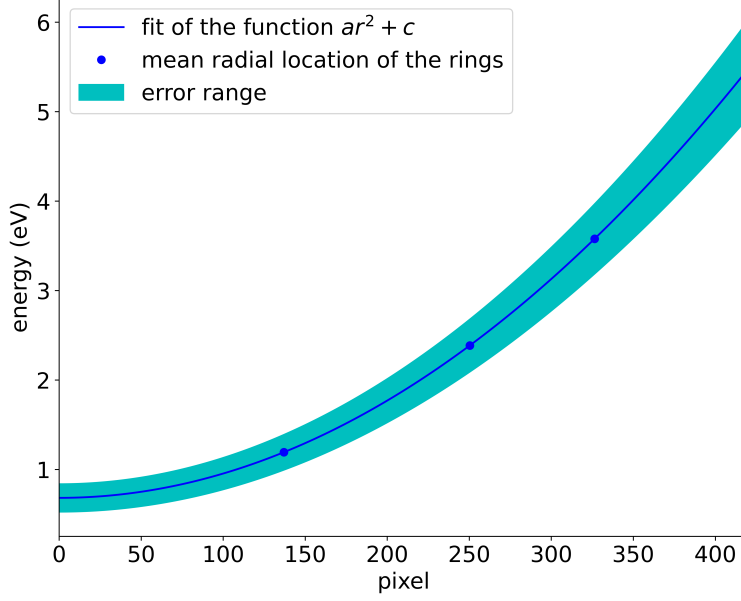
Figure 17: Energy calibration of the velocity-map imaging. The location of the rings is fitted to the energy of each ring $s\hbar\omega$, with s being the number of the ring, with the equation $ar^2 + c$ for each measured angle. The mean fit-values are used to fit Equation 55. The shaded area is the error range of the fit. The energy is shown in eV

at the position of the peaks is the multiple of the energy of the photons, therefore equals the energy of the first peak $\hbar\omega$ and the energy of the second peak $2\hbar\omega$ and so on. The energy of a photon of the laser frequency is 1.193 eV. A fit was done for each measured angle, where the energy of the rings was plotted against the radial position of the peaks. Thus, the energy offset c is a parameter to determine the energy offset of the rings to $(n + s)\hbar\omega$. The lowest ionization potential of xenon is 12.13 eV [30], therefore 11 photons are needed to ionize an electron of xenon. The ponderomotive shift can be calculated with

$$U_{\text{pond}} = n\hbar\omega - (I_{\text{P}} + c), \tag{57}$$

this equation is only valid for $s = 0$ and therefore also $r = 0$.

The mean a, the mean energy offset c and their standard deviation were determined, with the help of the fits. The Equation (55) is fitted in Figure 17 with the mean a and the mean energy offset c. The shaded area is the error range of the plot. The mean energy offset of the measurement is $0.68(16)$ eV. U_{pond} can be calculated with the measured value of c with Equation (57), the values for I_{P} and n are given above, the value of E was taken for $E(0)$, this leads to the result for U_{pond} of $0.32(16)$ eV.

Figure (18) shows the fitted energy offset for every polarization angle. The energy offset is except of the range, where the intensity of the image decreased and where the traces of the mean intensity inside the cavity decreased, nearly consistent between 0.7 eV and 0.8 eV. In the range where the energy offset drops, it drops about 40% to an average in this range of 0.46 eV. In this range, the energy also fluctuates more than for the other angles.

The theoretical value of the cavity for the ponderomotive was also calculated with the Equation (31). The peak power of the laser beam focus was calculated with

$$P_{\text{peak}} = \frac{P_{\text{avg}}}{\frac{f_{\text{rep}}t_{\text{p}}}{d}}, \tag{58}$$

where P_{avg} is the average power of the beam, f_{rep} the repetition frequency and the time of the pulse t_{p}. f_{rep} is 100 MHz, P_{avg} is 1581 W and t_{p} equals 208 fs. This leads to the result of
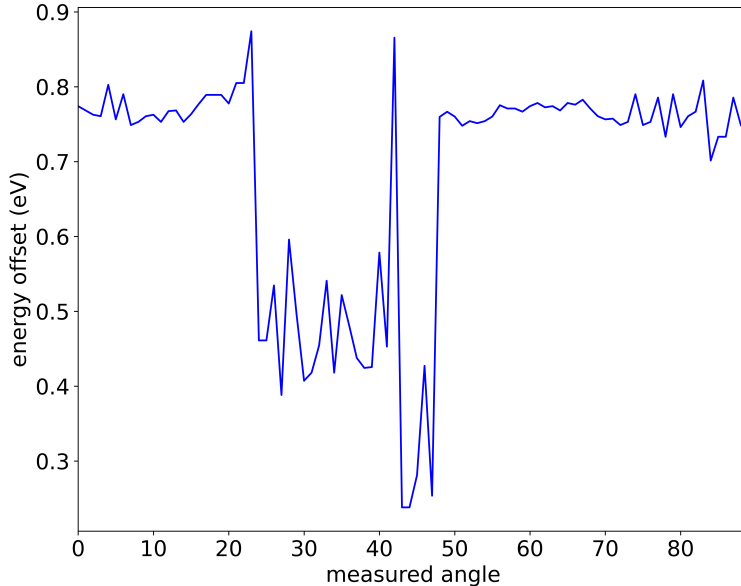
Figure 18: The energy offset c of all the measured angles from Equation (55). The energy is shown in eV. In the range of the measured angles 24 to 48, the energy drops drastically. U_{pond} increases when c decreases, this means that U_{pond} would be lower if the range where c drops would not be considered.

the Equation (58) of 7.6×10^6 W. With this peak power, an intensity of 6.05×10^{12} W cm^{-2} in the cavity focus is estimated. The resulting ponderomotive shift from Equation (31) is, therefore 0.609 eV. The value, which was calculated from the measurement, differs significantly from the theoretical value.

4.3   Comparison of Abel reconstruction and tomography

For the 3D-reconstruction of the electron emission, python is used. The inverse Abel transform of the images is applied with the pyabel package [4]. In order to produce a reconstruction of the electron momentum distribution, only one image of the p-polarization is needed for the inverse Abel transform. Here, the 'Basex' method is used for the inverse Abel transform. The Basex method is based on Gaussian basis set expansion [13]. Due to the assumption of the inverse Abel transform that the distribution is symmetrical, the output of the pyabel package is a cross-section of the reconstructed 3D-model. With the help of the package, it is possible to centralize the image. For the tomographic reconstruction, the iradon-package from python is used [2]. In order to perform the computer tomography the images had to be resized, thus the images were resized from (880×880) pixel to an image of (128×128) pixels. This package uses the filtered back projection algorithm. It calculates the Fourier transform and applies a frequency filter on the transform. Afterwards, it calculates the Inverse Fourier transform of the filtered projection. On the resulting cross-section, an interpolation is applied. Here, it is possible to use different interpolation methods.

4.3.1   Data from the Abel transform

The conditions of the Abel transform, that the distribution is cylinder symmetrical and that the symmetry axis is parallel to the detector, are met only with the p-polarization. On the image with the p-polarization, the electron rings of the distribution are clearly visible and identifiable. On the image where the laser was s-polarized, the electron rings are above each other. In a calibration, the number of the angle is determined where the laser is s-polarized,
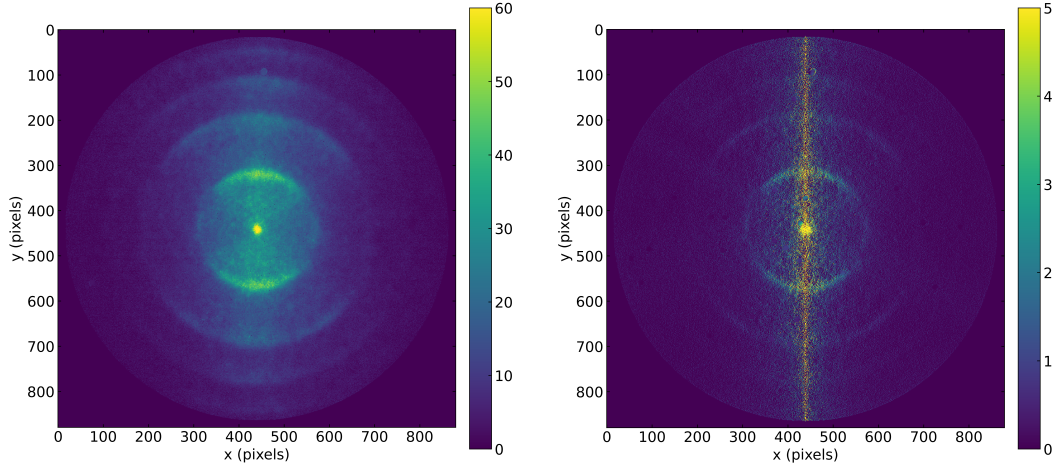
Figure 19: On the left is the measured image where the laser is p-polarization. On the right is the Abel transform of the same image, it is just a cross-section of the 3D-reconstruction, therefore is the intensity here much smaller. The line of bright spots in the middle of the Abel transform is due to the transformation, because there is the symmetry axis.

this is the 26th angle. Therefore, it is possible to determine the image where the laser is p-polarized, which is the 71st image. The Abel transform was applied on the 71st image. In Figure 19 is a comparison of the reconstructed image of the 71st angle on the left and the cross-section of the Abel transform of the same angle. The intensity of the cross-section is much smaller than the original image, because in VMI measurements, all the electrons are integrated above each other. Before the Abel transform, the image was centralized in order to have the middle of the distribution as the origin of the cylindrical coordinate system of the Abel transform to reduce errors of asymmetry. The strip in the image is due to asymmetrical errors in the middle, and they sum up and form the strip at the z-axis of the cylinder coordinate system. It is clearly visible that the electron clouds are in the same place and that the Abel transform is a good reconstruction of the electron momentum distribution.
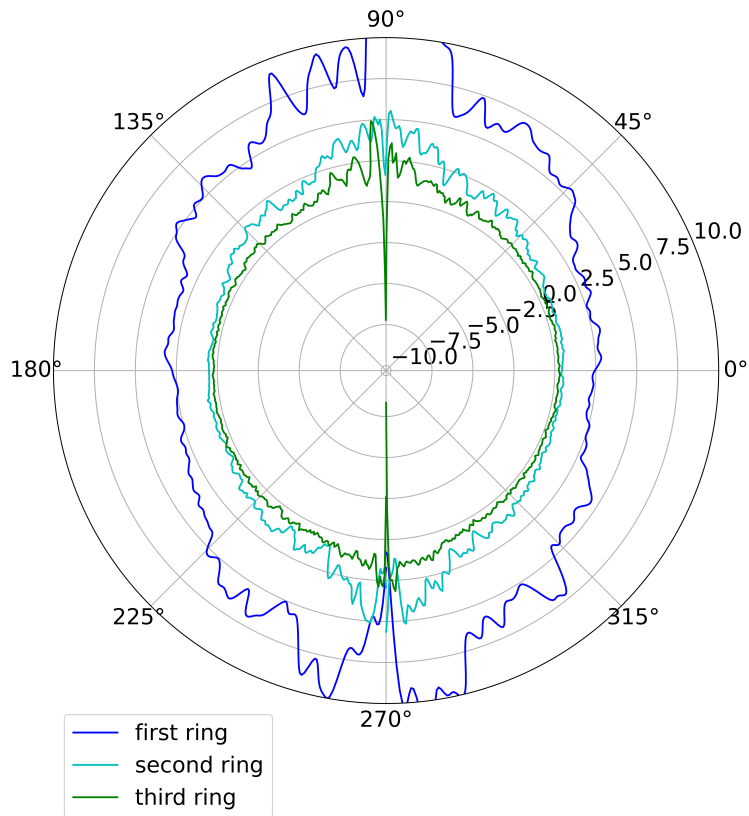
In Figure 20 is the intensity of the rings shown. The intensity of the rings from the Abel transform was integrated over the radius in order to get this plot. As expected, the intensity of the first ring is the highest and the intensity of the second ring is higher than the third ring. At the angle of 90° and at the angle of 270° is the z-axis, which is the symmetry axis of the Abel transform, which causes the minima in the intensity there. The minimum and the maximum next to it represent the line in the middle of the Abel transform.

In reality there is no negative intensity, thus the negative values are not scientific, but the result of the Abel transform. The angular distribution of photoelectrons can indicate the spin polarization([19]), but the angular intensity does not show any nodes. Because of that, no conclusions on the spin polarization can be made about the spin polarization of the photoelectrons from this data.
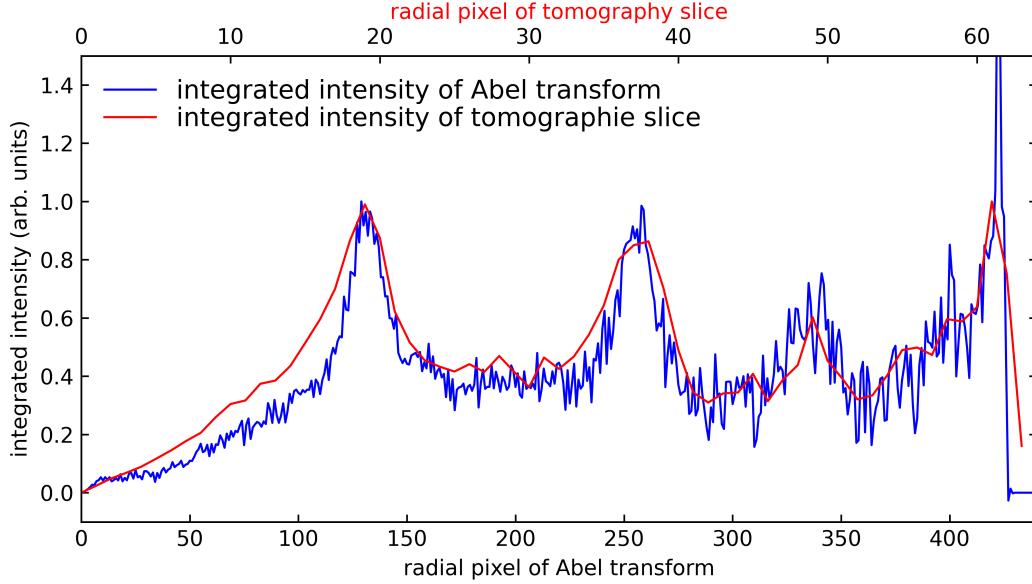
4.3.2 Intensity comparison between Abel transform and Computer tomography

Figure 21 shows a comparison of the radial intensity of the Abel transform and of a slice of the tomographic reconstruction. The slice of the tomographic reconstruction is taken out of the middle of the 3D-model. The x-axes are different, due to a resizing of the images for the Filtered Backprojection. The tomographic reconstruction is projected on 128 pixels. Therefore, the radius of each slice is 64 pixels. The peaks of the two reconstructions match

Figure 20: This polar plot presents the intensity of the rings of the electrons integrated over the radius of the rings of the Abel transform of the image with the p-polarized laser. The radial value is the intensity of the ring. The center of the plot is the center of the photoelectron momentum distribution.

Figure 21: A comparison of the integrated intensity along the radius between the cross-section of the Abel transform from the image where the laser is p-polarized and the slice of the computer tomography of the photoelectron momentum distribution.

each other, and the whole plot of intensity of the slice resembles the plot of the intensity of the Abel transform. In Figure 22, both images, the slice of the tomography and the cross-section of the Abel transform, are shown. The slice looks smeared due to the resizing, but the intensity of the pixels is much higher compared to the intensity of the pixels of the Abel transform. The rings of the electrons are more clearly visible on the slice, but on the cross-section they are more precise and more noisy.

4.3.3 3D-reconstruction

For the illustration of the computer tomography 3D-reconstruction two different methods were used, a scatter plot (Figure 25) and a plot with an isosurface (Figure 23 and 24). The python package pyabel which was used for the Abel transform gives only a slice out of the 3D-reconstruction of the electron momentum distribution, hence no 3D-model of the Abel transform is shown here.

The cross-section of the Abel transform is shown above in Figure 19. In both the tomographic representations only one ring is clearly visible. This visible ring corresponds to the second ring of the distribution. In the middle of the representation is a cloud, which reaches up to the first ring. The intensity is high between the center of the image and the first ring on all the images of the polarization angles, which produces this cloud. The third ring is only barely recognizable on the negative z-axis. There is noise around the distribution, caused by bright spots, which are only on some projections. Moreover, the representations are not cylinder symmetrical around the z-axis, as they should be. On the images of the s-polarization, the rings should be perfectly round, so that the view along the z-axis should be circles, which is not the case. This is one of the reasons of the missing symmetry. Additionally, the difference between an image with an artifact correction and reconstruction without the artifact correction is shown in Figure 26. The artifacts produce traces all around the electron momentum distribution. These traces are random around the distribution, without any symmetry. This confirmed that the artifacts do not belong to the electron momentum distribution.
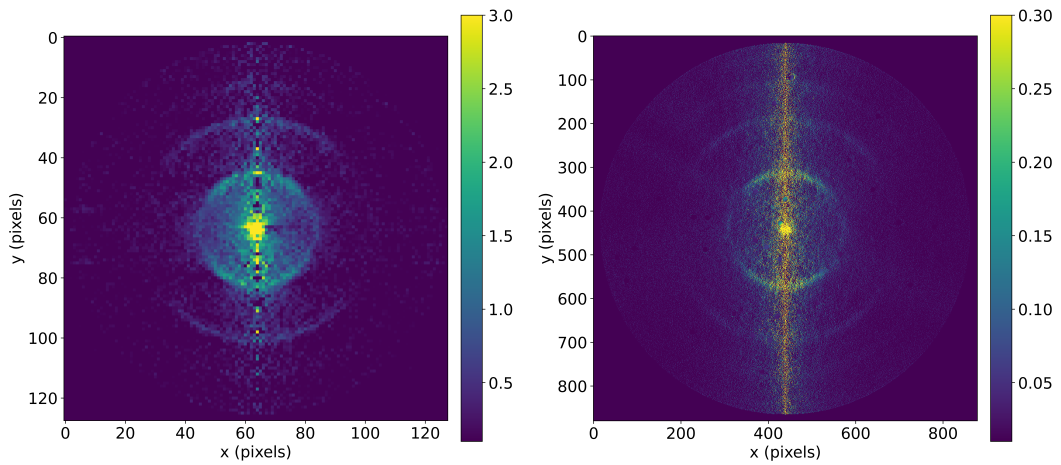
Figure 22: On the left is the slice of the tomographic reconstruction and on the right the cross-section of the Abel transform. The slice of the computer tomography is much more smeared due to the resizing for the Filtered Backprojection, because of the resizing is the brightness a bit higher than the cross-section of the Abel transform. The Abel transform is more fine and details are better recognizable than on the slice of the tomography.
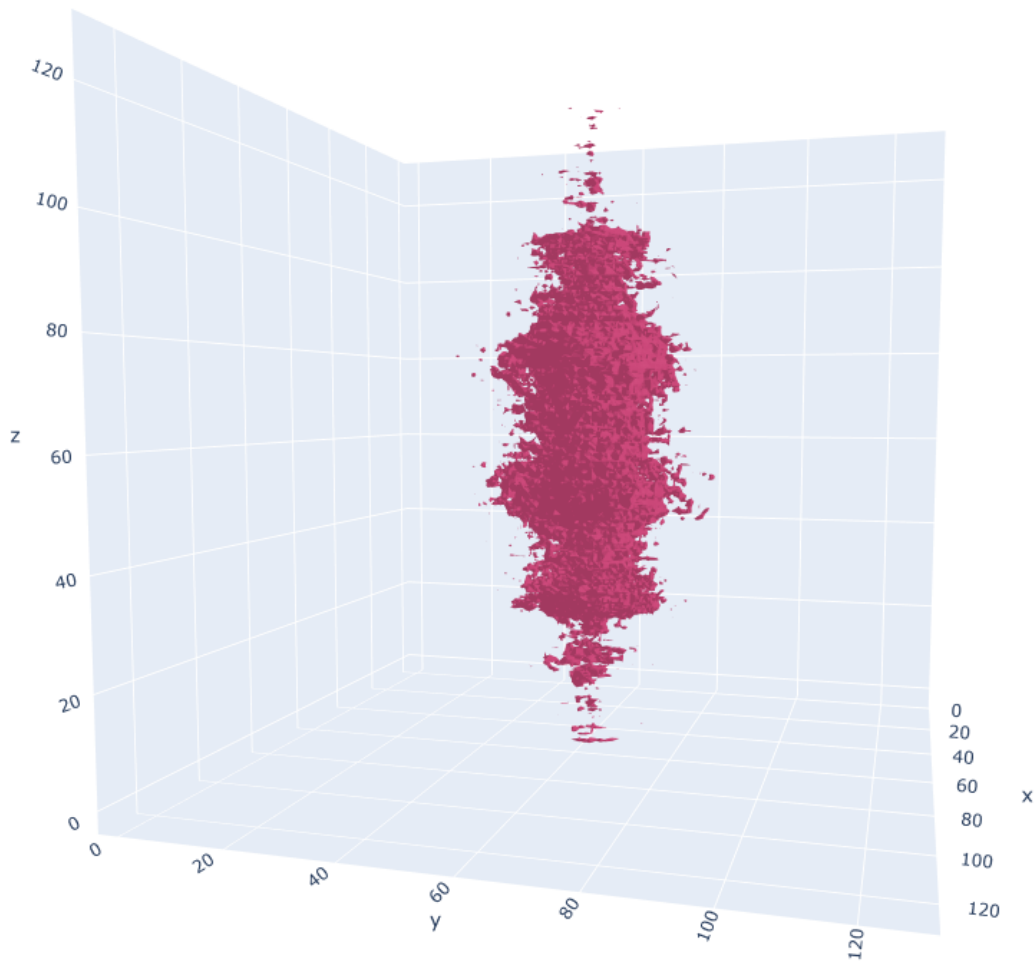
Figure 23: Here is the computer tomography plotted with the isosurface plot. It shows the electron momentum distribution from the side, where the first two rings are identifiable. The x-axis is parallel to the laser, the z-axis the direction of the s-polarization of the laser and the y-axis is along the p-polarization of the laser.
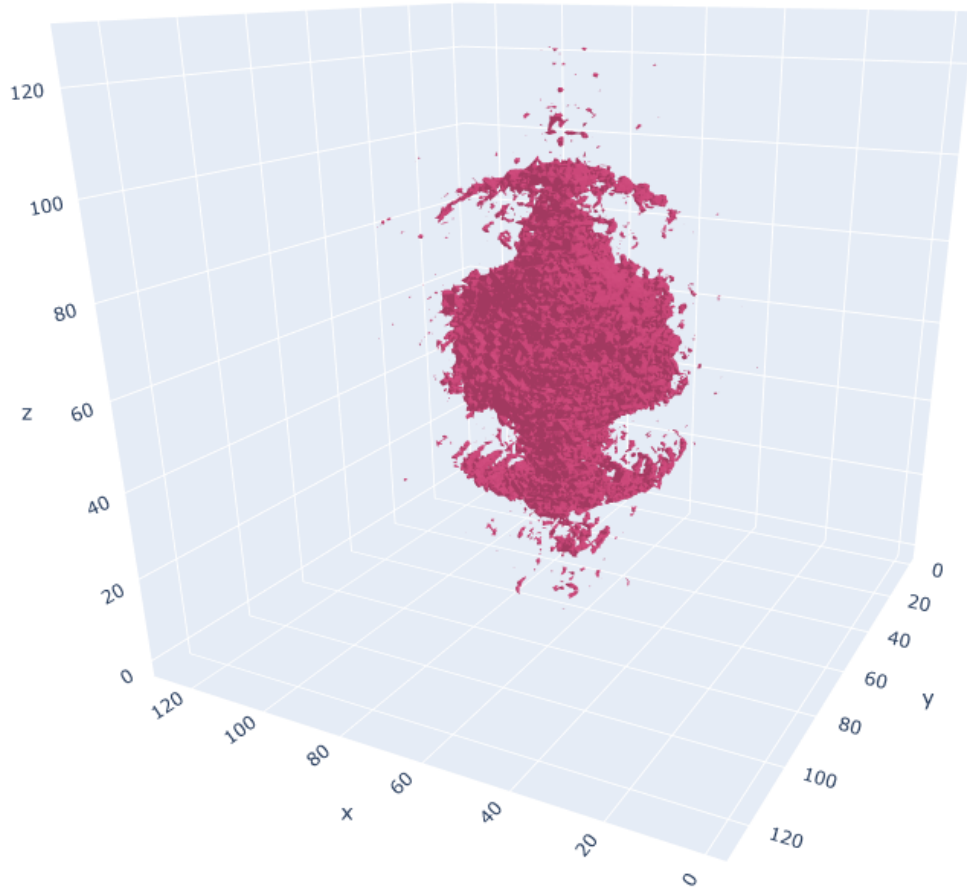
Figure 24: This figure shows the isosurface plot of the computer tomography of the electron momentum distribution from the front. The x-axis is parallel to the laser, the z-axis the direction of the s-polarization of the laser and the y-axis is along the p-polarization of the laser.
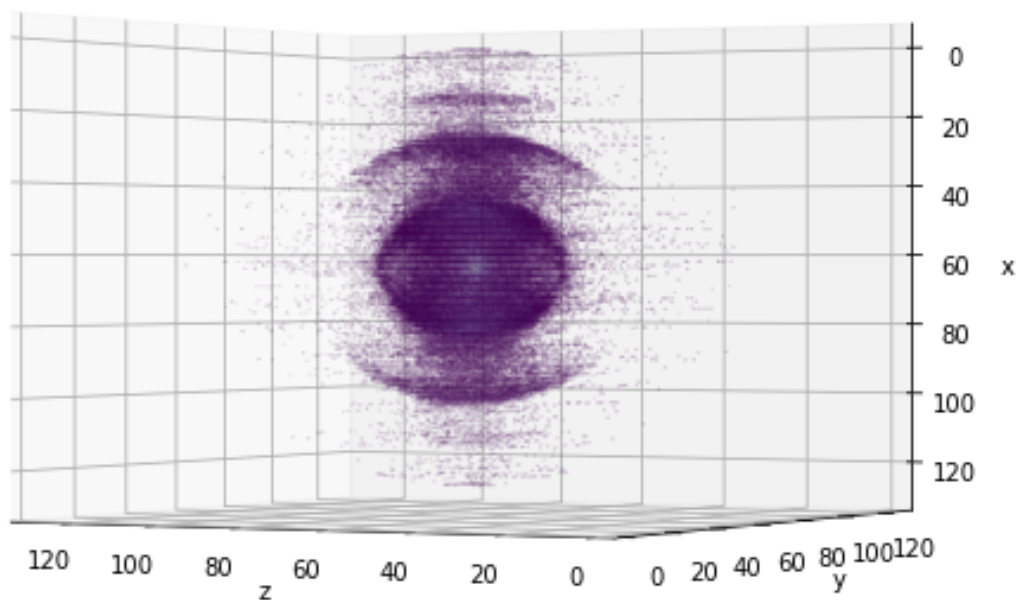
Figure 25: This figure illustrates the computer tomography of the xenon ATI photoelectrons with a scatter plot. Around the distribution is noise, but the first three rings are recognizable. The z-axis is in the direction of the laser, the x-axis is in the direction of the s-polarization and the y-axis is in the direction of the p-polarization.

(a)   (b)
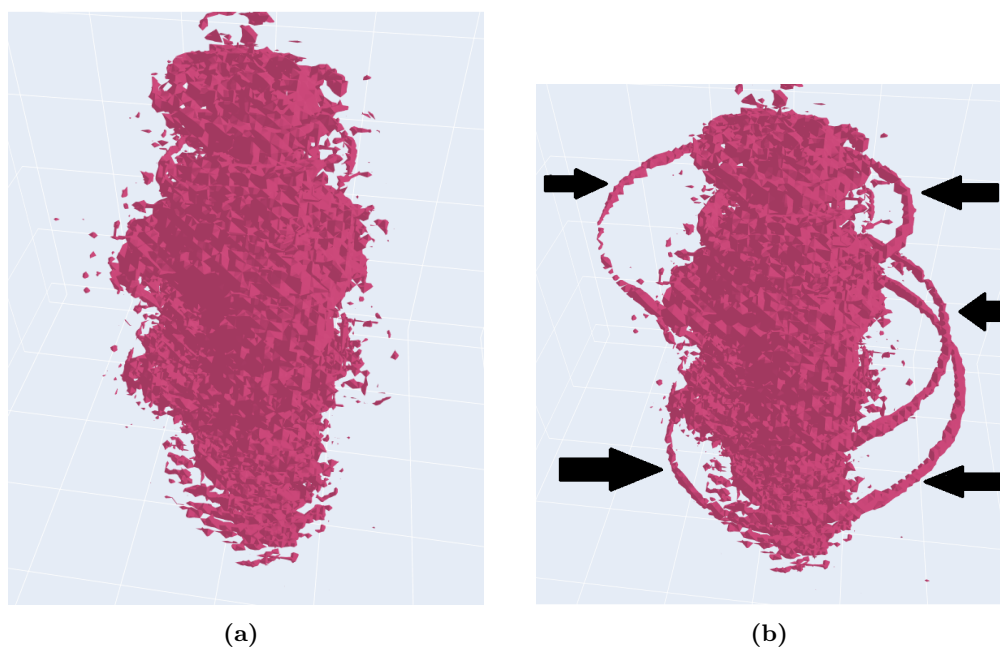
Figure 26: On the left is an image of the 3D-reconstruction with the artifact correction, on the right is the 3D-reconstruction with artifacts, which are pointed out with arrows. These images show the importance of the artifact correction, which is explained in section 4.3.3 .

5 Conclusion and Outlook

The goal of this thesis was the application of different 3D-reconstruction methods on a Velocity Map Imaging measurement in a femtosecond enhancement cavity. The VMI-setup was designed and produced beforehand, and the numerical characterization of the setup was done by Valentin Wössner in his bachelor thesis. He simulated measurements with VMI, used this data to characterize the VMI and to test the general idea of 3D-reconstruction through computer tomography.

At first the measured data was configured, in order to analyze the data and to do the 3D-reconstruction with computer tomography and inverse Abel transform. Many artifacts, which are caused by the MCP, were on the original measured images. These artifacts were edited out of the image with a least-square-fit, which significantly improved the reconstructed 3D-models. The images were investigated through plots of the integrated intensity. The intensity of the whole images fluctuate, hence the plots could be inaccurate. A reason for this is the inconsistent intensity inside the cavity during the measurement. With the help of these plots, the ponderomotive shift was determined, which was compared with the theoretical value for the used laser intensity. These two values agree in the range of two sigma. The determined value from the measurement is too small compared to the theoretical value, a reason for this is the intracavity power was not stable during the whole measurement and in the calculation for the theoretical value it is assumed that the laser power is constant. At last, the two reconstruction methods were compared. The Abel transform was performed with the Python package pyabel, the output of it is a cross-section of the 3D-model. The cross-section was compared to the actual image of the according polarization angle. The Abel transform is pretty similar to the original image, in the middle of the cross-section is just a bright line, which is not supposed to be there, along the symmetry axis of the Abel transform. The cross-section of the Abel transform was also compared to a slice of the computer tomography. In order to perform the computer tomography, the image was resized, thus the slice is smeared. The slice represents the original image well, although it is not as accurate as the Abel transform. Figure 22 showed that the radial reconstruction of both methods is equally good, both have the peaks and rings at the same radius. The advantage of the Abel transform is that only the angle of the p-polarization is necessary to recreate the distribution and that the reconstruction is very detailed, but it is also prone to noise on the image. The advantage of the computer tomography compared to the Abel transform is the independence of the exact polarization and the 3D-illustration, the noise is reduced in the computer tomography through the resizing which is another advantage, and therefore it is easier to show the basic structure of the distribution and it is more robust.

On the short term, the next step is to take more measurements with a stable intensity inside the cavity and to validate the results of the measurement and to improve with the new data the 3D-reconstructions. The VMI-setup is a new design, therefore it is important to get to know it better and get experience on how the data has to be processed and evaluated. On the long term, the aim is to use the femtosecond enhancement cavity to do computer tomography of vortex electron distributions and to do pump probe experiments with three pulses.

6 Acknowledgements

I like to say thanks to Josè Crespo for giving me the opportunity to write my bachelor thesis in his group. Also, I like to thank Alexander Dorn for doing the secondary correction. I want to thank the whole group of Josè for all the fun and welcoming me in the group and the cakes.

Especially, I want and need to thank Tobias Heldt and Jan-Hendrik Oelmann for being always there for me and my questions. You two showed what it means to do scientific work and so much more. I learned so much from the two of you, without your tips I would probably still be writing the thesis. Your love and passion for science inspired and motivated me during writing this thesis.

I want also to thank the 'Studentenbüro' for the friendship and making this time a good and fun memory. Many thanks to Ibi and Nick for proofreading this thesis. At last, I want to thank all my friends and family, who are always there for me. Your encouragement and support motivated and helped me a lot of writing this thesis.

References

[1] G-234b camera. `https://www.edmundoptics.de/p/allied-vision-mako-g-234b-112-monochrome-cmos-camera/3608/`. Accessed: 2022-02-06.

[2] iradon python package. `https://www.kite.com/python/docs/skimage.transform.iradon`. Accessed: 2022-02-06.

[3] Mcp-detector. `https://www.topag.de/produkte/messtechnik/mikrokanalplatten-&-detektoren/mcp-detektoren`. Accessed: 2022-02-06.

[4] pyabel python package. `https://pyabel.readthedocs.io/en/latest/abel.html#module-abel.tools.vmi`. Accessed: 2022-02-06.

[5] python program for data evaluation kernel description. `https://git.mpi-hd.mpg.de/XUV-Spectroscopy/VMI_II_Auswertung`. Accessed: 2022-02-06.

[6] *Fundamentals of Signal Processing*, pages 101–150. Springer Berlin Heidelberg, Berlin, Heidelberg, 2008.

[7] *Technical Implementation*, pages 241–301. Springer Berlin Heidelberg, Berlin, Heidelberg, 2008.

[8] *Two-Dimensional Fourier-Based Reconstruction Methods*, pages 151–200. Springer Berlin Heidelberg, Berlin, Heidelberg, 2008.

[9] Richard James Bentley-Moyse. *Towards Velocity Map Imaging: Implementation of a Self-Centering Inverse Abel Transform Script*. PhD thesis, MA thesis. University of Western Australia, 2014.(see p. 70).

[10] Eric D. Black. An introduction to pound–drever–hall laser frequency stabilization. *American Journal of Physics*, 69(1):79–87, jan 2001.

[11] David W. Chandler and Paul L. Houston. Two-dimensional imaging of state-selected photodissociation products detected by multiphoton ionization. *The Journal of Chemical Physics*, 87(2):1445–1447, jul 1987.

[12] Wolfgang Demtröder. *Experimentalphysik 2*. Springer-Verlag GmbH, March 2018.

[13] Vladimir Dribinski, Alexei Ossadtchi, Vladimir A. Mandelshtam, and Hanna Reisler. Reconstruction of abel-transformable images: The gaussian basis-set expansion abel transform method. *Review of Scientific Instruments*, 73(7):2634–2642, jul 2002.

[14] A. Einstein. Über einen die erzeugung und verwandlung des lichtes betreffenden heuristischen gesichtspunkt. *Annalen der Physik*, 322(6):132–148, 1905.

[15] André T. J. B. Eppink and David H. Parker. Velocity map imaging of ions and electrons using electrostatic lenses: Application in photoelectron and photofragment ion imaging of molecular oxygen. *Review of Scientific Instruments*, 68(9):3477–3484, sep 1997.

[16] F Fabre, Guillaume Petite, Pierre Agostini, and M Clement. Multiphoton above-threshold ionisation of xenon at 0.53 and 1.06 μm. *Journal of Physics B: Atomic and Molecular Physics*, 15(9):1353, 1982.

[17] R. R. Freeman, P. H. Bucksbaum, H. Milchberg, S. Darack, D. Schumacher, and M. E. Geusic. Above-threshold ionization with subpicosecond laser pulses. *Physical Review Letters*, 59(10):1092–1095, sep 1987.

[18] R. R. Freeman, T. J. McIlrath, P. H. Bucksbaum, and M. Bashkansky. Pondermotive effects on angular distributions of photoelectrons. 57(25):3156–3159, dec 1986.

[19] Keh-Ning Huang. Theory of angular distribution and spin polarization of photoelectrons. *Physical Review A*, 22(1):223–239, jul 1980.

[20] LV KELDYSH. Ionization in the field of a strong electromagnetic wave. *SOVIET PHYSICS JETP*, 20(5), 1965.

[21] R Kopold, W Becker, M Kleber, and G G Paulus. Channel-closing effects in high-order above-threshold ionization and high-order harmonic generation. 35(2):217–232, jan 2002.

[22] T. H. MAIMAN. Stimulated optical radiation in ruby. *Nature*, 187(4736):493–494, aug 1960.

[23] Eric Mbakop. *A historical perspective on quantum physics and its impact on society.* PhD thesis, Ph. D. dissertation, WORCESTER POLYTECHNIC INSTITUTE, 2009.

[24] J. Nauta, J.-H. Oelmann, A. Ackermann, P. Knauer, R. Pappenberger, A. Borodin, I. S. Muhammad, H. Ledwa, T. Pfeifer, and J. R. Crespo López-Urrutia. 100 MHz frequency comb for low-intensity multi-photon studies: intra-cavity velocity-map imaging of xenon. *Optics Letters*, 45(8):2156, apr 2020.

[25] Nathalie Picqué and Theodor W. Hänsch. Frequency comb spectroscopy. *Nature Photonics*, 13(3):146–157, feb 2019.

[26] Emiel Por, Maaike van Kooten, and Vanja Sarkovic. Nyquist–shannon sampling theorem. *Leiden University*, 1:1, 2019.

[27] J Radon. On the determination of functions from their integrals along certain manifolds. *Ber. Verh, Sachs Akad Wiss.*, 69:262–277, 1917.

[28] Dominic J. Ruggieri. Microchannel plate imaging detectors. *IEEE Transactions on Nuclear Science*, 19(3):74–84, 1972.

[29] E. Sakkoula, B. G. M. van Oorschot, and D. H. Parker. A compact electrostatic lens for velocity map imaging experiments. *Molecular Physics*, page e1910357, apr 2021.

[30] E. B. Saloman. Energy levels and observed spectral lines of xenon, $xe i through xe LIV$. $Journal of Physical and Chemical Reference Data, 33(3): 765 −−921, sep 2004.$

[31] C Smeenk, L Arissian, A Staudte, D M Villeneuve, and P B Corkum. Momentum space tomographic imaging of photoelectrons. *Journal of Physics B: Atomic, Molecular and Optical Physics*, 42(18):185402, sep 2009.

[32] Th. Udem, J. Reichert, T. W. Hänsch, and M. Kourogi. Accuracy of optical frequency comb generators and optical frequency interval divider chains. *Opt. Lett.*, 23(17):1387–1389, Sep 1998.

[33] Valentin Wössner. Tomographische rekonstruktion dreidimensionaler photoelektronenverteilungen mittels intra-cavity velocity map imaging, 2020.

[34] F Yergeau, G Petite, and P Agostini. Above-threshold ionisation without space charge. *Journal of Physics B: Atomic and Molecular Physics*, 19(19):L663–L669, oct 1986.

[35] A. M. Zheltikov. Keldysh parameter, photoionization adiabaticity, and the tunneling time. *Physical Review A*, 94(4):043412, oct 2016.

Erklärung:

Ich versichere, dass ich diese Arbeit selbstständig verfasst habe und keine anderen als die angegebenen Quellen und Hilfsmittel benutzt habe.

Heidelberg, den (Datum)